Inhibitory effect of lactoferrin-coated zinc nanoparticles on SARS-CoV-2 replication and entry along with improvement of lung fibrosis induced in adult male albino rats

Esmail M. El-Fakharany [a,*], Hamada El-Gendi [b,*], Yousra A. El-Maradny [a,c], Marwa M. Abu-Serie [d], Khaled G. Abdel-Wahhab [e], Marwa E. Shaban [f], Mahmoud Ashry [g]

[a] *Protein Research Department, Genetic Engineering and Biotechnology Research Institute (GEBRI), City of Scientific Research and Technological Applications (SRTA-City), New Borg El-Arab City 21934, Alexandria, Egypt*

[b] *Bioprocess Development Department, Genetic Engineering and Biotechnology Research Institute, City of Scientific Research and Technological Applications (SRTA-City), New Borg El-Arab City 21934, Alexandria, Egypt*

[c] *Microbiology and Immunology, Faculty of Pharmacy, Arab Academy for Science, Technology and Maritime Transport (AASTMT), Alamein 51718, Egypt*

[d] *Medical Biotechnology Department, Genetic Engineering and Biotechnology Research Institute (GEBRI), City of Scientific Research and Technological Applications (SRTA-City), New Borg El-Arab 21934, Alexandria, Egypt*

[e] *Medical Physiology Department, National Research Centre, Giza, Egypt*

[f] *Pathology Department, National Research Centre, Giza, Egypt*

[g] *Zoology Department, Faculty of Science, Al-Azhar University, Assuit, Egypt*

ARTICLE INFO

ABSTRACT

Severe acute respiratory syndrome 2019-new coronavirus (SARS-CoV-2) is a major global challenge caused by a pandemic disease, named 'COVID-19' with no effective and selective therapy available so far. COVID-19-associated mortality is directly related to the inability to suppress the viral infection and the uncontrolled inflammatory response. So, we investigated the antiviral efficiency of the nanofabricated and well-characterized lactoferrin-coated zinc nanoparticles (Lf-Zn-NPs) on SARS-CoV-2 replication and entry into host cells. Lf-Zn-NPs showed potent inhibition of the entry of SARS-CoV-2 into the host cells by inhibition of ACE2, the SARS-CoV-2 receptor. This inhibitory activity of Lf-Zn-NPs to target the interaction between the SARS-CoV-2 spike protein and the ACE2 receptor offers potent protection against COVID-19 outbreaks. Moreover, the administration of Lf-Zn-NPs markedly improved lung fibrosis disorders, as supported by histopathological findings and monitored by the significant reduction in the values of CRP, LDH, ferritin, and D-dimer, with a remarkable rise in CD4+, lung SOD, GPx, GSH, and CAT levels. Lf-Zn-NPs revealed therapeutic efficiency against lung fibrosis owing to their anti-inflammatory, antioxidant, and ACE2-inhibiting activities. These findings suggest a promising nanomedicine agent against COVID-19 and its complications, with improved antiviral and immunomodulatory properties as well as a safer mode of action.

1. Introduction

Severe Acute Respiratory Syndrome-Coronavirus-2 (SARS-CoV-2) is an enveloped RNA virus and a coronavirus disease (COVID-19) causative agent. Despite the available vaccination and treatment against SARS-CoV-2, there are about half a million cases worldwide daily, and the overall number of deaths from COVID-19 is over six million people worldwide [1]. Currently, vaccination is widely applied as a prophylactic strategy against COVID-19 infection [2]. However, the efficiency of vaccination and its applicability during pandemic conditions are still challenging [3]. Additionally, the high mutation rate in the RNA viruses increased the risk of multi-resistant variant development with more virulence characteristics. Hence, the need for an innovative, available, safe, and low-cost antiviral agent is mandatory. The relationship between severe COVID-19 infection and acute respiratory distress syndrome has been widely reported [4]. This condition may be complicated in some cases and develop into pulmonary fibrosis (known as post-COVID-19 pulmonary fibrosis), which usually requires intensive care

and oxygen supplementation [5]. The progressive consequences of pulmonary fibrosis (PF) usually lead to an inexorable decline in lung function, eventually leading to death [6]. Currently, two antifibrotics are approved for PF treatments, namely Pirfenidone and Nintedanib, but the clinical outcomes and cancer-developing potential challenge their application and enforce the search for more effective and safer alternatives [7–9].

Several studies reported the efficacy of lactoferrin protein and zinc supplements for the efficient co-treatment of COVID-19 patients [10–12]. The glycoprotein lactoferrin (Lf), which serves a variety of functions, including being a part of the innate immune response, is found in external secretions, including milk and other biological fluids [13]. Lf, a member of the transferrin family, is a monomeric 77.5–80 kDa protein made up of about 700 amino acids, which are folded into two globular lobes with a helix acting as a linker and a conserved iron-binding domain [14,15]. Lf has the highest affinity for ferric ions and can bind Cu^{2+}, Zn^{2+}, and Mn^{2+} ions. When iron is bound to Lf, it undergoes significant conformational changes, changing from its iron-free apo-lactoferrin (apo-Lf) form to either an open or closed state called holo-lactoferrin (ho-Lf) [16]. Lf possesses extensive antibacterial, antifungal, and virucidal action in addition to antioxidant, anticancer, and anti-inflammatory properties [17]. The mechanisms of antiviral activity of Lf are direct binding to viral proteins, blocking of virus entry receptors, or inhibiting viral enzymes [18,19]. However, *in vivo*, Lf stability and half-life time remain major challenges for successful application [20]. The Lf half-life time was estimated to be around 10–12.5 min, with complete removal from the human body after 7 h of injection [21]. Therefore, several studies reported the formulation of free Lf on specific carriers to enhance its stability and targeted release during *in vivo* applications [22–24].

Recently, a wide range of nanoparticles (NPs), particularly metallic nanoparticles, have been reported with excellent biological activities and drug-delivering characteristics [25,26]. The metallic nanoparticles possess solid structures and quick manufacturing processes, despite their non-biodegradable nature. Furthermore, the ability of most NPs to accumulate protein on their surfaces in corona-like structures facilitates their application in targeting protein delivery with lower cytotoxicity and higher efficiency [27,28]. Among others, zinc oxide-NPs (ZnO-NP) exhibit exceptional antimicrobial capability due to their increased specific surface area and increased surface reactivity brought on by their smaller particle size [29,30]. Additionally, recent research revealed ZnO-NP has effective inhibitory activity against a variety of viral diseases [31], including corona, herpes simplex [32], hepatitis E virus (HEV), hepatitis C virus (HCV) [33], and influenza [34]. However, the NPs' stability and tendency to accumulate biological molecules (especially during *in vivo* applications) challenge their application in the medical field [35]. Therefore, the current study aims to study the potential *in vitro* antiviral activity of green synthesized Zn-NPs when decorated with bovine Lf against COVID-19 infection. Additionally, the nano-composite will be evaluated *in vivo* for alleviating the PF progress in rat models, which is first reported, to the best of our knowledge.

2. Materials and methods

2.1. Purification, concentration, and molecular weight determination of lactoferrin

Bovine skim milk was prepared from raw milk according to methods of Almahdy et al. [36] with some modifications. In brief, bovine milk was defatted by centrifugation at 10,000 rpm for 30 min and decaseinated by decreasing the pH to about 4.2 with 5.0 % acetic acid. The skim milk was obtained after centrifugation at 4000 rpm for 20 min to precipitate casein proteins, and then the supernatant was dialyzed against a 50 mM Tris-HCl buffer pH 7.6 for 24 h. The purified bovine Lf was prepared from the obtained skim milk, as reported previously [37,38]. The obtained skim milk was applied to the pre-equilibrated Mono S 5/50

GL column, and Lf was eluted with 50 mM Tris-HCl buffer, pH 8.0, containing a NaCl gradient of 0.0–1.0 M. After dialysis, the pooled fractions of Lf were applied to a Sephacryl S100 column (5 × 150 mm, GE Health Care, Sweden) equilibrated with 50 mM Tris-HCl buffer, pH 7.6, and eluted with the same buffer containing 150 mM NaCl. Also, the obtained pooled fractions of Lf were applied to a heparin-sepharose column (affinity chromatography) equilibrated with 50 mM Tris-HCl buffer, pH 7.6, and eluted with the same buffer containing a NaCl gradient of 0.0–1.0 M. For the preparation of apo-Lf, about 50 mg/mL protein was dissolved in double distilled water (ddH_2O) and dialyzed extensively for 24 h against 100 mM citrate buffer, followed by dialysis against ddH_2O for another 24 h, as previously reported [39]. The purity and molecular weight of Lf were estimated by SDS-PAGE. The purified Lf fractions were pooled, dialyzed, lyophilized, and kept at −80 °C until use, whereas protein concentration was determined according to the Bradford method [40]. The molecular weight of the purified lactoferrin was tested using native polyacrylamide gel electrophoresis (PAGE) and SDS-PAGE, as described by Laemmli [41].

2.2. Preparation and characterization of lactoferrin-zinc-NPs

2.2.1. Preparation of zinc nanoparticles (Zn-NPs)

Zinc nanoparticles (Zn-NPs) were synthesized according to [42] with some modifications. In brief, 0.5 g of zinc acetate solutions were prepared on a magnet stirrer in 10 mL of 1 M NaOH. Afterward, 0.55 g of ascorbic acid powder (Sigma Aldrich, USA) was added under stirring for 20 min, and the pH was finally adjusted to 7.0 with 0.1 M HCl. The generated Zn-NPs were separated through centrifugation (10,000 rpm for 10 min) and then washed three times with ddH_2O.

2.2.2. Preparation of lactoferrin-zinc-NPs

Lactoferrin-zinc nanoformulations (Lf-Zn-NPs) were prepared by mixing the purified Lf in 0.1 M sodium bicarbonate with a two-fold excess of the prepared Zn-NPs for 2 h under stirring. The mixture was extensively dialyzed against 0.1 M sodium bicarbonate to remove free metal ions. After dialysis, the obtained protein nanoparticle complex was lyophilized (solid white powder) and used as a source for Lf-Zn-NPs. The zinc content and Lf in the prepared nanocomplex were estimated using the atomic absorption technique and Bradford spectrophotometric method at 595 nm [40], respectively.

2.2.3. Characterization of the formulated Lf-Zn-NPs

The prepared Zn-NPs and Lf-Zn-NPs were characterized using the Zetasizer (ZS 6.2, Malvern, Germany) to evaluate their hydrodynamic sizes, distribution, and net surface charge (Zeta potential) for the prepared particles. The crystal structure in the prepared NPs was evaluated through X-ray diffraction (XRD) using X PERT PRO-PAN Analytical (Netherlands) in the range of 5° to 80° at 2θ with a scan rate of 5°/min. The morphological characteristics of the prepared particles were evaluated through scanning electron microscopy (SEM) at 5000× using a JSM 6360LA electron microscope (Tokyo, Japan).

2.2.4. Evaluation of Zn-NPs and Lf-Zn-NPs cytotoxicity

The cytotoxicity of the prepared Zn-NPs and Lf-Zn-NPs against normal lung cells Wi-38 and SARS-CoV-2 host cells (Vero E6) in comparison to the free Lf was determined using the (3-(4,5-dimethylthiazol-2-yl)-2,5-diphenyltetrazolium bromide) tetrazolium reduction assay (MTT assay). All normal cells (1.0×10^4 cells/well) were seeded into 96-well sterile plates and cultivated in Dulbecco's modified Eagle's medium (SERANA, Germany) supplemented with fetal bovine serum (10 % Gibco, New York, NY, USA) and 1 % Pen/Srep mixture (Lonza, USA) for overnight. Cells were treated with various concentrations of each free compound and nanoformulation, and the cytotoxicity of the compounds against normal cells was determined using the MTT method (Mosmann, 1983). After 48 h of incubation, 200 μL of MTT solution (0.5 mg/mL; Sigma, USA) was added to each well, and the plate was incubated at

37 °C for 2–5 h. After removing the MTT solution, 200 μL of dimethyl sulfoxide (DMSO) was added to each well, and absorbance at 570 nm was measured using a microplate reader (BMG LabTech, Germany). The half-maximal inhibitory concentration (CC_{50}) and safe dose (EC_{100}) values of the tested compounds were determined using GraphPad InStat software 7.

2.2.5. Determination of endotoxin concentrations of Zn-NPs and Lf-Zn-NPs

The endotoxin (ET) concentrations in each formulated sample were determined using an endotoxin ELISA kit (Sunlong Biotech Co., Ltd) following the manufacturing protocol. Briefly, the micro-ELISA plate wells were filled with standard or NPs samples. Then, avidin conjugated to a horseradish peroxidase (HRP)-conjugated antibody specific for ET was added to each well. After washing, the TMB substrate solution was applied to each well. The optical density (OD) was measured spectrophotometrically at 450 nm, where ET concentrations (pg/mL) were calculated from a standard curve with a sensitivity range of 0.0156–1.00 EU/mL.

2.3. Quantification of Lf-Zn-NPs binding and internalization

2.3.1. Lf-Zn-NPs binding

The binding of the prepared Lf-Zn-NPs to Vero E6 cells plasma membrane was evaluated by indirect immunofluorescence as compared to free Lf [43]. Briefly, after seeding Vero E6 cells for 24 h, serial concentrations of free Lf, Zn-NPs, and Lf-Zn-NPs were incubated for 1 h at 4 °C. Afterward, cells were washed three times in cold phosphate-buffered saline (PBS). Cells were incubated with rabbit anti-Lf immunoglobulins for 60 min, and then washed five times with cold PBS. The fluorescein isothiocyanate (FITC)-conjugated anti-rabbit gamma globulin antibodies were added for 60 min to stain the cells. Then, cells were washed again and fixed with 3.7 % paraformaldehyde in PBS containing 2 % sucrose for 10 min at room temperature. Cells were then washed twice in PBS and incubated for 10 min at room temperature in 0.5 % Triton X-100 in the same buffer containing 10 % sucrose. After washing five times in PBS, the cellular binding of Lf was measured at 520 nm emission and 490 nm excitation using a fluorometer (BMG LabTech, Germany).

2.3.2. Assessment of cellular internalization of the prepared NPs

The cellular internalization of the prepared NPs was evaluated in the Vero E6 cell line through the fluorescein isothiocyanate (FITC) staining method [44]. First, the Zn-NP and free Lf were tagged with FITC through the dropwise addition of 50 μL of FITC (1 mg/mL dissolved in DMSO) into 0.5 mg/mL of the Zn-NPs stock solution (4.8 nM in ddH$_2$O) under constant stirring in dark conditions at 4 °C. After 12 h, ammonia was added to a final concentration of 50 mM. The mixture was then incubated again for 2 h at 4 °C before glycerol (25 % *v/v*) was added. The reaction mixture was centrifuged at 10,000 rpm for 45 min before being washed with ddH$_2$O to separate the untagged FITC. Vero E6 cells were cultured for 24 h in DMEM medium supplemented with 10 % fetal bovine serum (FBS) in a 5 % CO$_2$ incubator at 37 °C. The supernatant media were removed, and then 100 mg/mL of the FITC-conjugated Zn-NPs, Lf, and Lf-Zn-NPs were added, whereas NPs cellular internalization at different time intervals was examined at 488 nm using flow cytometry analysis (Partec, Germany).

2.4. In vitro antiviral activity of Lf-Zn-NPs against SARS-CoV-2

2.4.1. Anti-SARS-CoV-2 assay

Vero E6 cells were utilized to propagate the authentic SARS-CoV-2 virus (accession number: KC869678.4), and the cells were harvested after the appearance of cytopathic effects (CPE). The viral stocks were then titrated using the plaque infectivity assay and the MTT method, based on the median tissue culture infectious dose (TCID50), and stored at −80 °C until further use. In order to evaluate anti-SARS-CoV-2

activity of the biosynthesized Zn-NPs and the prepared Lf-Zn-NPs, Vero E6 cells were seeded in 24-well culture plates (10^5 cells/well) at 37 °C and 5 % CO2 for 24 h. previously titrated SARS-CoV-2 virus for 1 h and then mixed with a safe doses (EC_{100}) of each tested compound. For the neutralization mode, each tested compound (Lf, Zn-NPs or Lf-Zn-NPs) at different concentrations (0–100 μg/mL, 2 fold) was mixed with the virus and kept at 37 °C for 1 h before being added to the 80–90 monolayers cells after the removal of the growth medium and then the virus/compound mixtures were inoculated in triplicates for another 1 h. For the post-infection mode, Vero E6 cells were infected with the virus for 1 h at first, then washed 3 times with fresh media for removing unbound viral particles and exposed to each compound at different concentrations as mentioned above. Remdesivir was used as antiviral drug at different concentrations (0.0 to 100 μg/mL). Both positive and negative controls were included through viral infection of the untreated cells or use healthy cells (virus untreated cells) in each plate, respectively. One mL of DMEM with 1 % Pen/Strep, and 2 %FBS were added to each well and incubated for 48 h at 37 °C and 5 % CO2. Supernatants were harvested and the viral load was measured in each sample using viral 1-Step RT-qPCR. The curve of viral neutralization (for neutralization mode) and the curve of viral inhibition (for post-infection mode) of each tested compound against SARS-CoV-2 were plotted using Graph Pad Prism 7.0 and the IC$_{50}$ values (50 % inhibitory concentrations) were calculated from the non-linear regression curve-fit analysis.

2.4.2. RT-qPCR

Viral RNA extraction was performed from 1.0 mL of cell culture supernatants with the Quick-RNA Viral Kit (cat. # R1035, Zymo Research, USA) according to the protocol provided by the manufacturer. The viral RNA was eluted in 50 μL of nuclease-free water. SARS-CoV-2 genome detection and quantification were performed with the TaqMan Fast Virus 1-Step Master Mix System (cat. # 4444434, Applied Biosystems) using specific primers targeting SARS-CoV-2 E protein at 6 pmol (each) and probe at 5 pmol per reaction. Forward primer sequence: ACAGGTA CGTTAATAGCGT; reverse primer: ATATTGCAGCAGTACGCACACA; and probe: FAM-ACACTAGCCATCCTTACTGCGCTTCG-BBQ. The PCR mix containing Master Mix, primers and probe was incubated with 6 μL of an 1:50 (*v/v*) dilution of sample RNA. Cycling was conducted in Applied Biosystems 7500 Real-Time PCR System. The reactions were incubated at 50 °C for 10 min for reverse transcription, and 95 °C for 2 min, followed by incubation at 95 °C for 5 s and 60 °C for 30 s for data collection over 45 cycles. A plasmid containing SARS-CoV-2 E protein amplicon was used as standard curve in order to establish an absolute quantification of viral RNA copies per mL of supernatant.

2.4.3. The inhibitory influence on SARS-CoV-2

The inhibition of SARS-CoV-2 through the prepared Lf-Zn-NPs was evaluated compared to Zn-NPs and free Lf by testing their ability to inhibit three key factors in the life cycle of SARS-CoV-2, including binding to the ACE2 receptor, Cathepsin L (Cat L), and RNA-dependent RNA polymerase (RdRp). First, the inhibition of the ACE2 receptor was evaluated according to the manufacturer's instructions for the ACE2/SARS-CoV-2 spike inhibitor screening kit (BPS Bioscience, #79936) at various concentrations (200, 100, 50, and 25 μg/mL). The concentration-response curve for the SARS-CoV-2 spike (1–100 nM) was created according to [45], and luminescence was measured using a FluoStar Omega microplate reader (BMG LabTech, Germany). On the other hand, the inhibition of viral infusion was evaluated through a Cathepsin L inhibitor screening kit (AssayGenie, #BN00441). Additionally, the inhibition of RNA synthesis in SARS-CoV-2 was evaluated through the RNA-dependent RNA polymerase commercial fluorescence kit (SARS-CoV-2 RdRp TR-FRET Assay kit). This kit was used to evaluate the possible inhibitory influence of the prepared LF-Zn-NPs on the activity of RNA-dependent RNA polymerase (RdRp). RdRp operates as a mixture of NSP7, NSP8, and NSP12 proteins. RdRp is a crucial enzyme in the life cycle of SARS-CoV-2 and is considered one of the most promising

druggable targets for SARS-CoV-2. The present kit contains Digoxigenin-labeled RNA duplex, biotinylated ATP, RdRp assay buffer (2 components plus DTT), and purified RdRp mixture proteins. The assay counts the amount of biotinylated ATP that is directly incorporated into the double-stranded RNA substrate. The rise in the TR-FRET signal is inversely related to the incorporation of ATP into the RNA. Only two steps are needed to detect RdRp activity with this kit. The reaction mixture's enzyme is first treated with a test substance. After adding the dye- and eu-labeled acceptor and antibody, the TR-FRET signal is read.

2.5. In vivo investigation of the Lf-Zn-NPs effect on pulmonary fibrosis (PF) modeled rats

2.5.1. Experimental animals and PF induction

This study was conducted on adult male Wistar albino rats (150–200 g) obtained from the Animal Colony, of the National Research Centre (NRC, Cairo, Egypt). The animals were housed in suitable plastic cages for one week for acclimation. Excess tap water and standard rodent pellets were always available. All animals received human care in compliance with the standard institutional criteria for the care and use of experimental animals, according to the NRC ethical committee. For PF induction, male Wistar albino rats were intratracheally injected with Bleomycin hydrochloride (2.5 mg/kg body weight in 0.25 mL PBS) as described previously [46]. The rats were sacrificed 29 days after the Bleomycin injection. Control animals received the same volume of intratracheal saline instead of Bleomycin.

2.5.2. Study animal groups

After PF induction, both normal and PF-modeled rats were randomly divided into five groups of 10 rats each. Group (1) served as controls; group (2) Bleomycin-induced PF animals served as positive controls (BLM) injected intratracheally with 2.5 mg/kg/weekly for six weeks; and groups (3), (4), and (5) PF-modeled animals that were treated with free Lf, Zn-NPs, and Lf-Zn-NPs, respectively, each at 50 mg/kg/day for six weeks.

2.5.3. Blood and tissue sampling

At the end of the treatment period, rats were weighed, then each animal was fasted overnight. Following anesthesia (sodium pentobarbital 9.1 mg/kg diluted in sterile 0.9 % NaCl, *via* IM injection), blood specimens were withdrawn from the retro-orbital plexus using heparinized and sterile glass capillaries; whole blood specimens were cool-centrifuged at 1000 rpm for 10 min, and the sera were separated, divided into aliquots, and stored at −80 °C. After blood collection, the animals were sacrificed, whereas the lungs were dissected. One part of the lung was washed in saline, dried, rolled in a piece of aluminum foil, and stored at −80 °C for biochemical determinations. Another portion of the lung was soaked in formalin-saline (10 %) buffer for histopathological processing and microscopic examination.

2.5.4. Complete blood count assessment

A cell blood counter (Model PCE-210 N, Japan) was used for measuring red blood corpuscles (RBCs) count ($10^6/cm^3$), hemoglobin (Hb) content (g/dl), hematocrit (HCT) percentage, platelet (PLT) count ($10^3/cm^3$), and total leukocyte (TLC) count ($10^3/cm^3$).

2.5.5. Evaluating of lung and oxidative stress biomarkers

ELISA kits (Sunlong Biotech Co., China) were used to measure lung biomarkers in rats, including C-reactive protein (CRP), ferritin, D-dimer, lactate dehydrogenase (LDH), fibronectin (FN), granulocyte-macrophage colony-stimulating factor (GM-CSF), and transforming growth factor beta (TGF-β). The microplates were read using a microplate reader (Dynatech, MR-5000). Additionally, ELISA kits (Sunlong Biotech Co., China) were used to measure lung glutathione (GSH), malondialdehyde (MDA), and nitric oxide (NO) levels, as well as superoxide dismutase (SOD), catalase (CAT), and glutathione peroxidase (GPx) activity in modeled rats. The microplates were read using a Dynatech Microplate Reader Model MR 5000.

2.5.6. Evaluation of pro-inflammatory cytokines and apoptotic biomarkers

Tumor necrosis alpha (TNF-α), interleukin-1 beta (IL-1β), interleukin-4 (IL-4), interleukin-6 (IL-6), interleukin-10 (IL-10), and CD4+ levels in rats were measured using ELISA kits (Sunlong Biotech Co., Hang Zhou, China). The microplates were read using a Dynatech Microplate Reader Model MR 5000.

2.5.7. Histopathology

Regarding histopathological assessment, lung samples from all groups were dissected immediately after being sacrificed. The specimens were then fixed in 10 % neutral-buffered formalin-saline for at least 72 h. All the specimens were washed in tap water for half an hour and then dehydrated in ascending grades of alcohol, cleared in xylene, and embedded in paraffin. Sections were cut (5-μm thick) and stained with hematoxylin and eosin (H&E) for histopathological investigation and for evaluating inflammatory cell filtration, congestion, collagen deposition (fibrosis), and alveolar thickening. These were graded into four classes: normal (0), weak (1), moderate (2), or intense (3), and the averages were considered. For each slide, the average of six fields was determined at a magnification of 100× (Kalantar et al., 2021). Images were captured at the pathology lab, National Research Centre, using the image analysis system Leica QWin DW3000 (LEICA Imaging Systems Ltd., Cambridge, England), which consists of a Leica DM-LB microscope with a JVC color video camera attached to a computer system and processed using Adobe Photoshop version 8.0.

2.5.8. Statistical analysis

The obtained data were subjected to a one-way ANOVA followed by Turkey multiple *post hoc* tests at a level of $p \leq 0.05$ using statistical analysis system (SAS) software. The correlation coefficient was applied to the present data using the SPSS software package (version 9).

3. Results
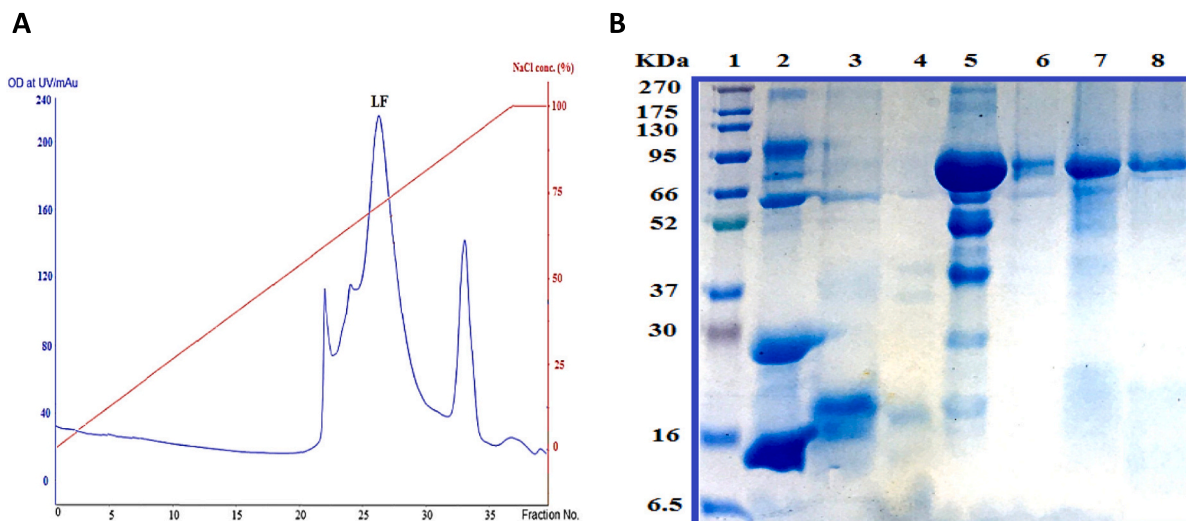
3.1. Purification of lactoferrin

Defatted bovine milk was prepared by centrifugation at 10,000 rpm for 30 min at 4 °C, and bovine skim milk was obtained by casein removal from defatted milk after decreasing the pH of skimmed milk to 4.2 with 5.0 % acetic acid. Bovine Lf was purified from skimmed milk in three simple steps: bovine skimmed milk was applied to a Mono S column, and Lf was eluted at a NaCl gradient of 0.3–0.7 M (Fig. 1 A). The eluted Lf in the third peak was confirmed by immunoassay using an anti-human lactoferrin antibody. All fractions containing Lf were pooled, concentrated, and applied to the Sephacryl S100 column. Then all fractions containing Lf were collected and applied to the heparin-sepharose column to obtain the protein with high purity. Homogeneity of the purified Lf was visualized by 12 % SDS-PAGE and corresponded to a molecular weight of 80 kDa for Lf (Fig. 1 B).

3.2. Green synthesis of Zn-NPs

Zinc nanoparticles (Zn-NPs) were prepared using a green approach through the reduction of zinc acetate (ZA) salts with ascorbic acid (vitamin C). To optimize the nanoparticles' size and oxygen percentage, several trials were carried out (changing vitamin C amount and pH range) during the green synthesis of Zn-NPs. As a result, adding 0.55 g of vitamin C with continuous stirring for 20 min and a pH of 7.0 were the optimum conditions for Zn-NPs.

3.3. Preparation of Lf-loaded Zn-NPs

For the preparation of Lf-loaded Zn-NPs, the purified Lf was

A

B

Fig. 1. A typical elution profile of bovine lactoferrin during purification on a Mono S column chromatography (A) with 12 % SDS-PAGE of the purified bovine lactoferrin during purification steps (B). Lane 1, molecular mass marker; lane 2, skim bovine milk; lanes 3 and 4, the eluted fractions from the first peak of Mono S 5/ 50 GL column; lane 5, the eluted Lf in the second peak of Mono S 5/50 GL column; lane 6, the eluted Lf from Sephacryl S100 column; lane 7, the eluted Lf from the heparin-sepharose column and lane 8, purified Lf protein.

incubated at various concentrations with 0.005 mg of Zn-NPs. The results indicated that 1 mg Lf was completely bound to Zn-NPs, whereas at higher Lf concentrations (1.2, 1.4, 1.6, 1.8, and 2 mg/mL), the binding percentage decreased to be ≤86.66 %, 69.68 %, 59.05 %, 48.84 %, and ≤ 40.05 % (Table 1). Hence, the optimal dose (1 mg/mL) of Lf was incubated with serial concentrations of Zn-NPs to detect the maximum (saturated) concentration of Zn-NPs on Lf protein, where the unbound Zn-NPs were separated through the centricon. At 0.5 mg of Zn-NPs, it was observed that 100 % of the NPs were chelated by Lf (Table 1). As was shown, at 1, 1.5, 2, and 2.5 mg, about 49 %, 64 %, 74 %, and 79 % of Zn-NPs were overabundant, respectively (Table 1).

3.4. Characterization of the prepared Zn-NPs and Lf-Zn-NPs

The characteristics of the green synthesized Zn-NPs were evaluated through a different instrumental analysis where the particle shape indicated a globular or spherical shape of Zn-NPs, as indicated in the SEM results (Fig. 2A and B). On the other hand, the particle sizes were around 55.91 nm, and their zeta potentials were − 21.62 mV (Fig. 2E). The EDX spectrum of zinc NPs confirmed the presence of an intense signal for zinc with a low signal for oxygen (Fig. 2D) at their corresponding surface energies of 8.630 keV. In Zn-NPs, EDX revealed the presence of 96.54 % Zn and 3.46 % oxygen at 8.0 and 0.5 keV, respectively. The phase identity, purity, and crystalline nature of zinc NPs were illustrated by XRD (Fig. 2C). As demonstrated, three distinct intense peaks with Bragg's reflection 101, 102, and 103 correspond to zero-valent Zn (JCPDS PDF #00–004-0831) in zinc NPs. On the other hand, the Lf-Zn-NPs indicated a rough surface with spherical-shaped

Table 1
The binding percentages of serial concentrations of Lf to Zn-NPs and the unbinding percentages of Zn-NPs after incubating with 1 mg Lf.

Lf (mg/mL)	Zn-NPs binding (%)	Total added Zn-NPs (mg) to 1 mg/mL of Lf	% Unbinding Zn-NPs
2	40.05 ± 4.66	0.5	0 ± 0
1.8	48.84 ± 2.99	1	49.35 ± 0.65
1.6	59.05 ± 3.35	1.5	64.87 ± 5.13
1.4	69.68 ± 3.12	2	74.62 ± 0.475
1.2	86.66 ± 1.55	2.5	79.24 ± 0.76
1	99.01 ± 0.54	–	–

All data are expressed as mean ± standard error of the mean (SEM).

structures. The particle sizes increased to 230.8 nm, with higher negatively charged surface structures (−36.85 mV) compared to those of Zn-NPs (Fig. 2F and H).

3.5. The endotoxin determination

The concentration of the tested preparations, their OD (450 nm), and the endotoxin (ET) concentration are presented in Fig. 3A. These results showed that the ET is concentration-dependent; as concentration decreases, the ET concentration also decreases. Zn-NPs showed the highest ET concentrations at 200 and 100 μg/mL. Lf showed the lowest ET concentration at all tested concentrations. The combination of Zn-NPs and Lf decreases the ET in Zn-NPs to be within the accepted range (0.5 EU/mL). Thus, the addition of Lf could help modulate the effect and increase the safety of used NPs.

3.6. Assaying the cytotoxicity of nanoparticles on cultured cells

The cytotoxicity of the prepared Lf-Zn-NPs was evaluated in Vero E6 cells as compared to free Zn-NPs and Lf. The results (Fig. 3B) revealed that coating the purified Lf with the biosynthesized Zn-NPs significantly blocked its cytotoxic effect on Vero E6 cells, compared to the uncoated Zn-NPs. The highest CC_{50} values were recorded in free Lf, followed by Lf-Zn-NPs at 1371 and 969.5 μg/mL, respectively, whereas free Zn-NPs showed the lowest CC_{50} value (145.1 μg/mL). Based on MTT findings, the tested Lf-Zn-NPs slightly impacted all normal cell viability in a concentration-dependent manner (Fig. 3C). Furthermore, our results indicate that the coating the purified Lf protein with Zn-NPs increased their safety in the treated normal cell lines with EC_{100} value >100 μg/mL. Fig. 4 confirms these trends of great safety of the prepared Lf-Zn-NPs on the treated Vero E6 cells by capturing the changes that occurred before and after treatment with all prepared samples at different concentrations using inverted phase contrast images *via* optical microscopy.

3.7. Internalization and cellular uptake of Lf-Zn-NPs

The cellular localization profiles of Zn-NPs, free Lf, and Lf-Zn-NPs reflect their biodistribution and transport efficiency. This study used flow cytometry to track the cellular absorption of NPs and protein-NP nano-complexes in Vero E6 cells at different time intervals (Fig. 5). This study showed that the cellular uptake of Zn-NPs and Lf-Zn-NPs is
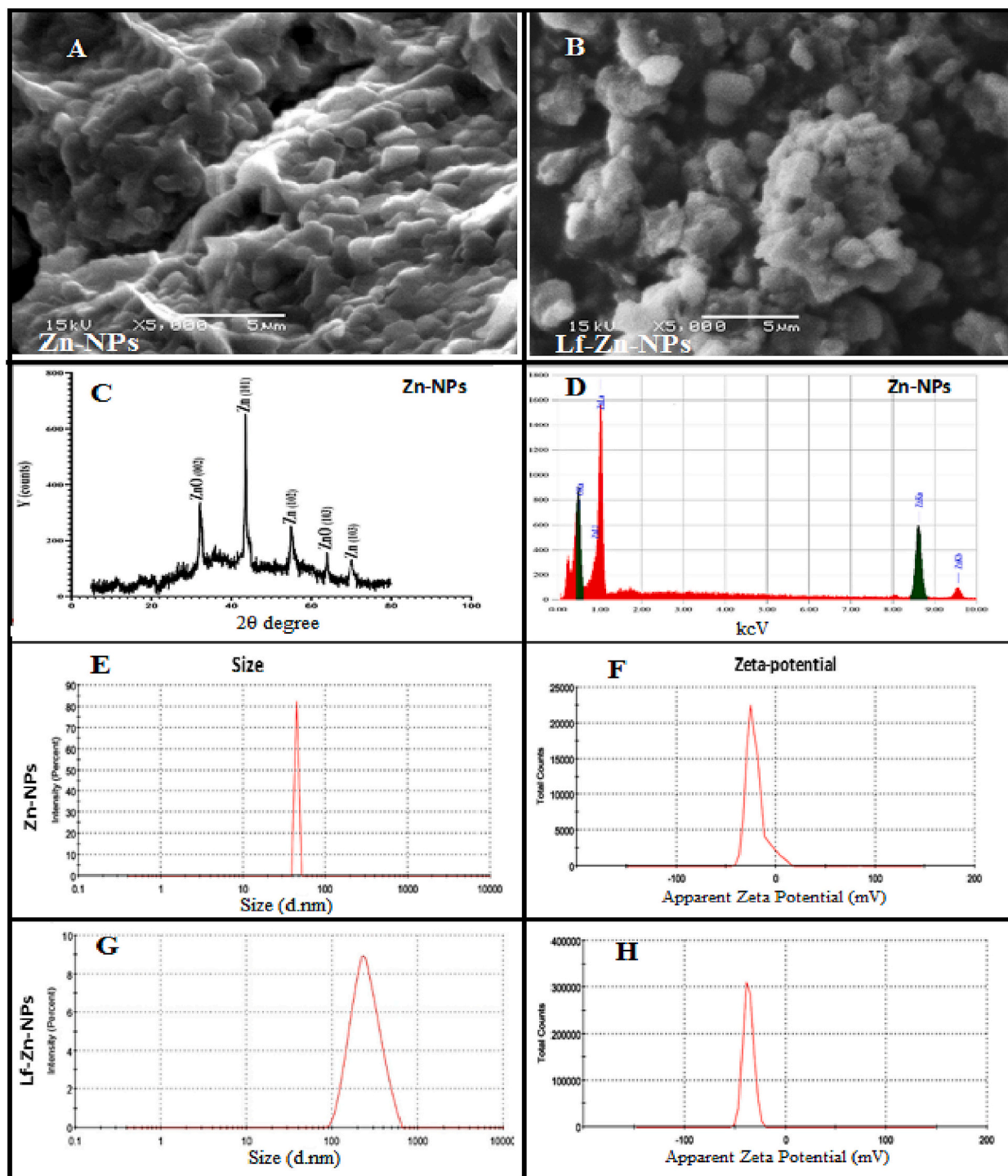
Fig. 2. (A and B) Representative SEM micrographs of Zn-NPs and their nano-complexes with Lf (Lf-Zn-NPs), respectively, at a magnification of 5000 X. (C) is the X-ray diffraction charts of Zn-NPs, where (D) is its elemental analysis charts (EDS). Zetasizer-generated data for the zeta size of Zn-NPs and their nano-complexes with Lf (E and G). Zetasizer-generated data for the zeta potential of Zn-NPs and their nano-complexes with Lf (F and H).

highly dependent on the time of incubation with cells. The fabrication of Zn with Lf showed better cellular uptake than Lf alone. These findings suggest that Zn-NPs facilitate and increase Lf internalization over time.

3.8. Evaluation of the activity of Lf-Zn-NPs against SARS-CoV-2

3.8.1. In vitro anti-SARS-CoV-2 assessment

The antiviral activity of Lf, Zn-NPs and Lf-Zn-NPs was assessed against SARS-CoV-2 using the Vero E6 cells after adding different

concentrations of these compounds to the healthy cells. Viral inhibition Efficacy for each compound were evaluated by quantification of viral copy load in the cell supernatant using qRT-PCR. The nanofabricated Lf-Zn-NPs exhibited a strong antiviral activity against SARS-CoV-2 rather than the biosynthesized Zn-NPs and Lf. Fig. 6A shows that Lf, Zn-NPs and Lf-Zn-NPs neutralized the viral particles with IC_{50} values of 39.97, 27.44 and 16.84 μg/mL, respectively compared to 12.37 for remdesivir. Also, it was found that Lf, Zn-NPs and Lf-Zn-NPs were able to inhibit the propagation of SARS-CoV-2 inside the viral-infect cells (post-infection
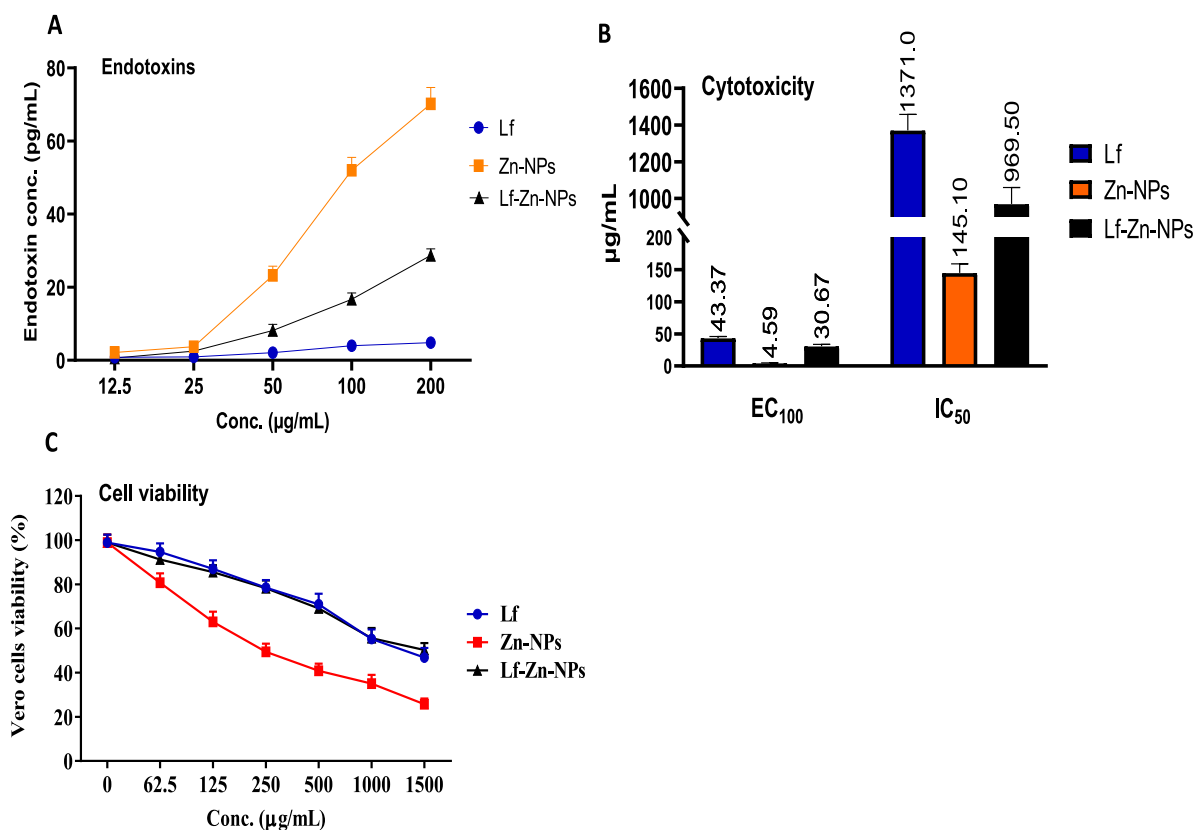
Fig. 3. EC_{100} and CC_{50} (µg/mL) and SI values of all tested Zn and Lf-Zn-NPs samples against the Vero cell line (A), where (B) is the general endotoxin (pg/mL) of the Zn and Lf NPs at different concentrations. Cytotoxicity evaluation on Vero cells (C) at different concentrations before and after treatment with the prepared material samples as compared to Lf. All values were expressed as mean ± SD, *n* = 3.

mode) with IC_{50} values of 34.98, 20.93 and 13.56 µg/mL, respectively compared to 11.24 µg/mL for remdesivir (Fig. 6B).

3.8.2. ACE2/SARS-CoV-2 spike inhibitor screening assay

An ACE2/spike inhibitor screening kit was used to detect the ability of the tested components to inhibit the ACE2/spike interaction. To verify the concentration-dependent rise in luminescence, a standard curve of different concentrations of the SARS-CoV-2 spike was performed. Free Zn-NPs were effective in blocking the binding of spike RBD to ACE2 in a dose-dependent manner over a concentration range of 25–200 µg/mL, revealing an estimated IC_{50} value of 89.73 ± 1.59 µg/mL. As presented in Fig. 7A, free Lf caused a slight and dose-dependent inhibition in the spike-ACE2 interaction with a high IC_{50} value of 1757 ± 1.02 µg/mL. The fabrication of Zn-NPs into Lf protein greatly enhanced the binding activity of Lf on the spike/ACE-2 with an IC_{50} value of 334 ± 2.23 µg/mL.

3.8.3. Cathepsin L inhibitory effect of Lf-Zn-NPs

The inhibitory effects of Lf-Zn-NPs, Zn-NPs, and free Lf on Cat L were studied using a fluorometric inhibitor screening kit and FF-FMK as an irreversible positive inhibitor control (1 mM). The results, presented in Fig. 7B, showed that Lf-Zn-NPs displayed a significant inhibitory effect against Cat L with an IC_{50} value of 139.6 µg/mL. On the one hand, Zn-NPs and free Lf had higher IC_{50} values (326.8 ± 9.818 and 188.5 ± 3.731 µg/mL, respectively) and hence a weaker inhibitory effect on Cat L.

3.8.4. RNA-dependent RNA polymerase (RdRp) inhibition

The inhibition of RNA synthesis in SARS-CoV-2 was evaluated through the RNA-dependent RNA polymerase commercial fluorescence kit. The results (Table 2) revealed a significant potential for Lf-Zn-NPs to

suppress the enzymatic activity of SARS-CoV-2 RdRp, compared to Zn-NPs and free Lf. This activity (94.57 ± 7.3 %) was even more than the remdesivir activity (91.78 ± 7.45 %) at 100 µg/mL. The IC_{50} value of Lf-Zn-NPs (28.29 ± 2.36 µg/mL) was significantly lower than that of remdesivir (67.52 ± 5.31 µg/mL), which asserted the ability of Lf-coated Zn-NPs to interfere and arrest viral replication at lower concentrations, compared to remdesivir as a standard antiviral drug and free Lf or Zn-NPs.

3.8.5. In vivo effect of the Zn-NPs and Lf-Zn-NPs on the PF-rat model

The treatment effects of Zn-NPs and Lf-Zn-NPs on pulmonary fibrosis were evaluated in an albino rat model upon injection with Bleomycin. The rats were allocated to five groups, including one untreated (BLM group) and three treated groups (Zn-NPs, free Lf, and Lf-Zn-NPs treated groups), with one healthy group (control group) as a negative control. The results indicated a significant drop in Hb (10.82 ± 0.18 g/dL), HCT (31.5 ± 0.55 %), and RBC (4.7 ± 0.32 10^6/µL) levels, with significant increases in the WBC (14.33 ± 2.7 10^3/µL), and platelet counts as a consequence of Bleomycin intoxication (untreated group) compared to the control group. The administration of Lf-Zn-NPs to Bleomycin-injected rats restored the hematological parameters to near-normal levels, as indicated in Table 3.

Furthermore, the pulmonary fibrosis-modeled animals showed a significant and marked increase in levels of CRP (39.2 ± 5.4 mg/L), ferritin (820 ± 62 ng/mL), LDH (4687 ± 194 U/L), D-dimer (1.3 ± 0.24 ng/mL), FN (150.4 ± 7.3 ng/L), GM-CSF (241 ± 29 ng/L), and TGF.β (1015 ± 50 ng/L) compared with the healthy group (4.5 ± 1.4 mg/L, 555 ± 28 ng/mL, 2451 ± 145 U/L, 0.12 ± 0.01 ng/mL, 64.5 ± 4.5 ng/L, 130 ± 15.3 ng/L, and 403 ± 40 ng/L). Interestingly, Lf-Zn-NPs significantly improved the levels of the biomarkers in the lung, which were close to those of the control group (14.08 ± 1.9 mg/L, 595 ± 37 ng/mL,
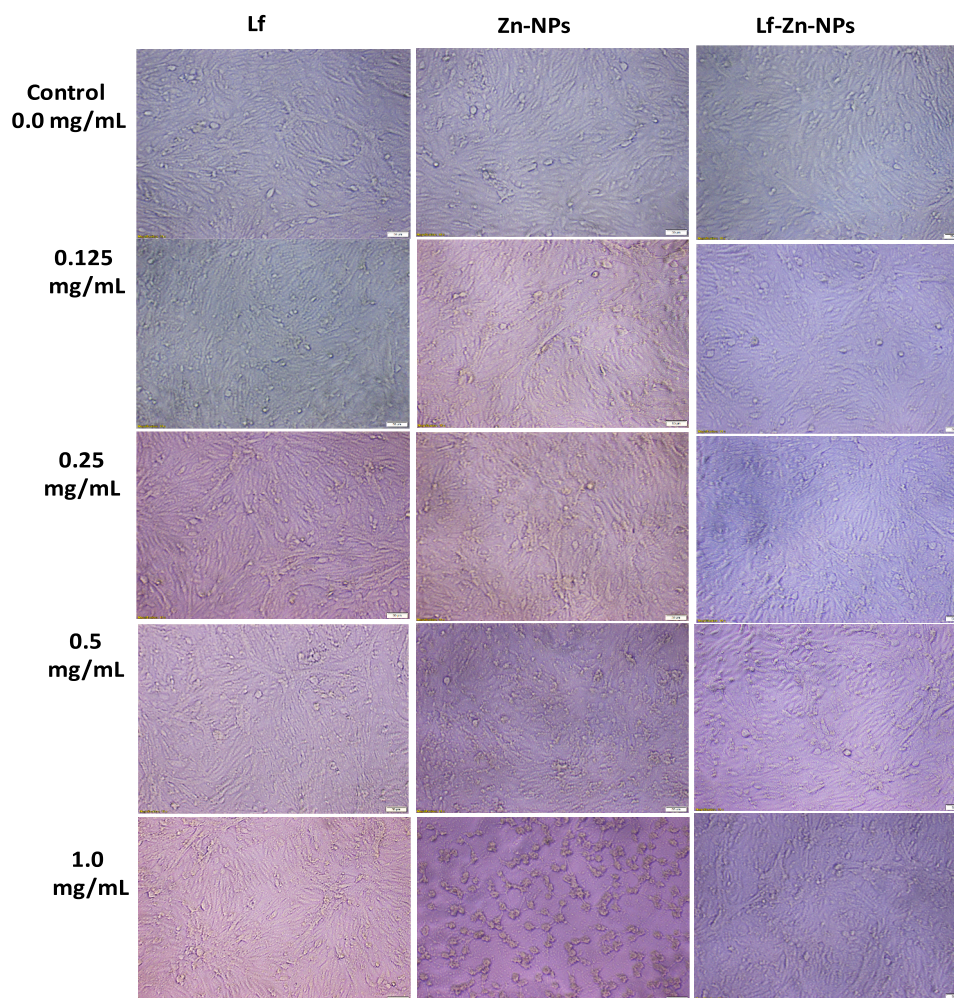
Fig. 4. Effects of BNES on morphological modifications of normal Vero cell line under phase contrast microscope. Vero E6 cells were treated with the prepared Zn-NPs and Lf-Zn-NPs at concentrations of 0.0 mg/mL (control), 0.125 mg/mL, 0.25 mg/mL, 0.5 mg/ mL, and 1.0 mg/mL. The scale bar in all images is 500 mm.

2736 ± 184 U/L, 79.3 ± 6.4 ng/mL, 0.55 ± 0.02 ng/L, 79.3 ± 6.4 ng/L, 149 ± 13 ng/L, 582 ± 50 ng/L) as indicated in Fig. 8(A–G).

Moreover, rats with induced pulmonary fibrosis revealed sharp disturbances in the oxidative status of lung tissues, as evidenced by the marked drop in values of the antioxidant enzymes (GSH, SOD, CAT, and GPx) matched with a significant increase in the oxidative biomarkers (MDA and NO) when compared with the healthy group. Fortunately, treatment of pulmonary fibrosis-modeled rats with Lf-Zn-NPs resulted in a significant decompensation of the depleted lung GSH content and upregulated the activity of lung CAT, GPx, and SOD. The Lf-Zn-NPs successfully reduced lung MDA and NO levels when compared to the corresponding values in the pulmonary fibrosis-modeled animal group (Table 4). Furthermore, rats with pulmonary fibrosis had significantly higher levels of serum pro-inflammatory cytokines, such as tumor necrosis factor-alpha (TNF-α), interleukin-1 beta (IL-1), interleukin-4 (IL-4), interleukin-6 (IL-6), and interleukin-10 (IL-10), when compared to the control group. Injection of Lf-Zn-NPs into the pulmonary fibrosis-modeled rats significantly alleviated these lung fibrosis deteriorations (Fig. 9A–F).

Histopathological examination.

As shown in Fig. 10, the staining of specimens indicated the normal structure of pulmonary parenchyma with an apparent intact alveolar epithelium and thin interalveolar septa with no accumulation of extracellular matrix (Fig. 10A). On the contrary, lung tissue of the group exposed to BLM was severely affected with a decreased number of alveoli, a significant thickness of alveolar septa, chronic bronchitis,

interstitial lung pneumonia, as well as marked and extensive infiltration of lymphocytes in the alveolar wall with lymphoid aggregates, inflammatory cell infiltration, marked fibrosis, interstitial hemorrhage, and dilated congested alveolar capillaries compared to the control group (Fig. 10B and C). The BLM groups treated with Lf, Zn-NPs, or Lf-Zn-NPs showed significant reductions in interalveolar wall thickness and reversed most of the induced injuries with some variation, such as the presence of scattered inflammatory cells and increased alveolar wall thickness in the Lf-treated group (Fig. 10D), while minimal fibrosis and increased alveolar wall thickness were observed in the Zn-NPs treated group (Fig. 10E). The best results were obtained with Lf-Zn-NPs, which demonstrated normal lungs (Fig. 10F). Furthermore, Table 5 shows the scoring of fibrosis and inflammation of lung tissues; the examination revealed that congestion, inflammation, alveolar thickness, and fibrosis were markedly increased in the lung fibrosis-modeled-animals' group in comparison to the healthy or normal animals' group. Interestingly, treatment of lung-fibrosis-modeled-animals with Zn-NPs alone or formulated with lactoferrin (Lf-Zn-NPs) resulted in a significant decrease in the scoring of congestion, inflammation, alveolar thickness, and fibrosis compared to the untreated fibrotic group. These results indicated that the prepared Lf-Zn-NPs exhibited the highest degree of improvement002E.

4. Discussion

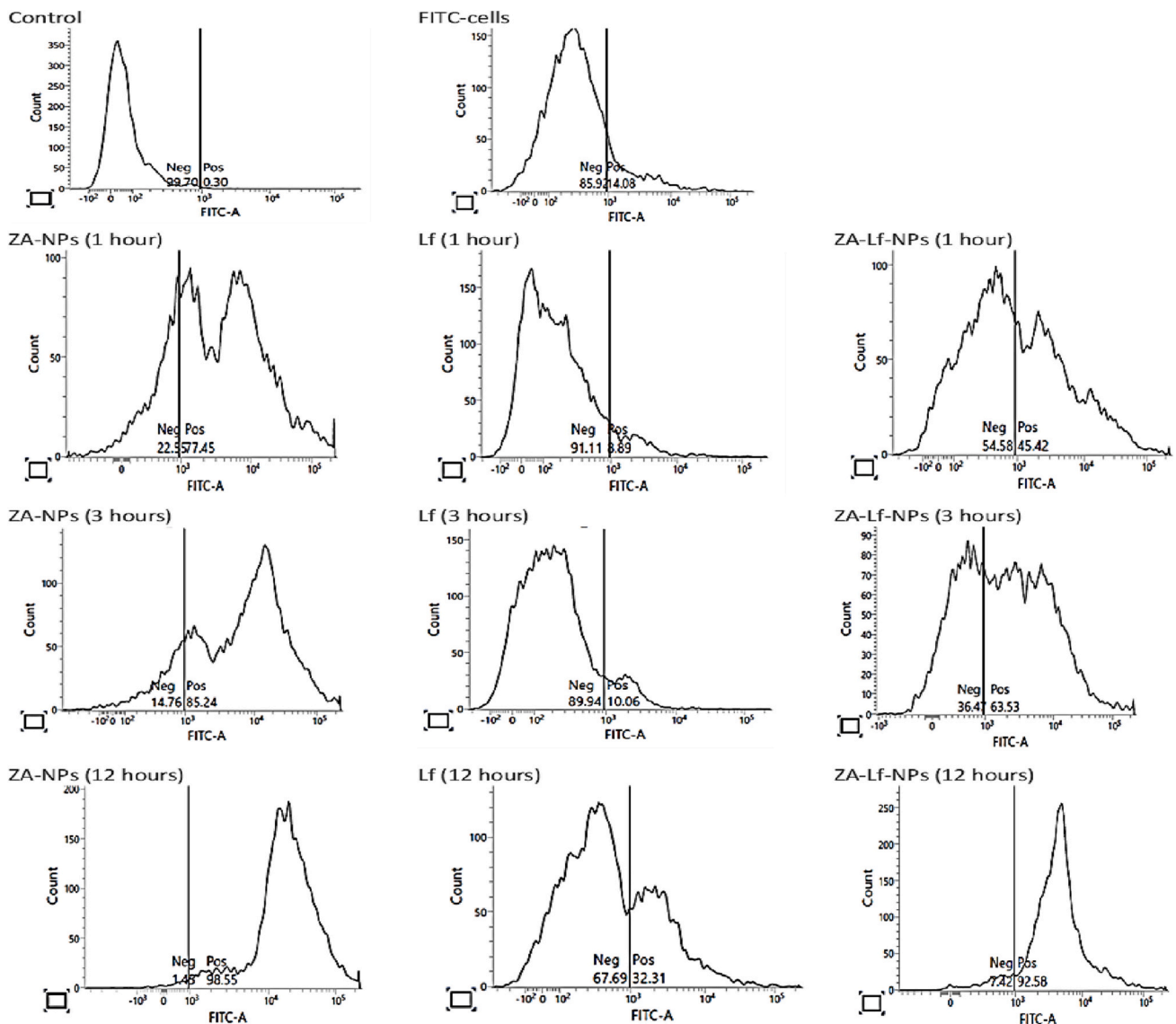There is a growing interest in the NPs' applications as antiviral drug

Fig. 5. Flow cytometry studies of cellular uptake of the prepared nanoparticles by viable Vero E6 cells. The cellular uptake was evaluated at different time intervals (12, 3, and 1 h) with 100 mg/mL of Zn-NPs, Lf, and Lf-Zn-NPs conjugated to fluorescein isothiocyanate (FITC).
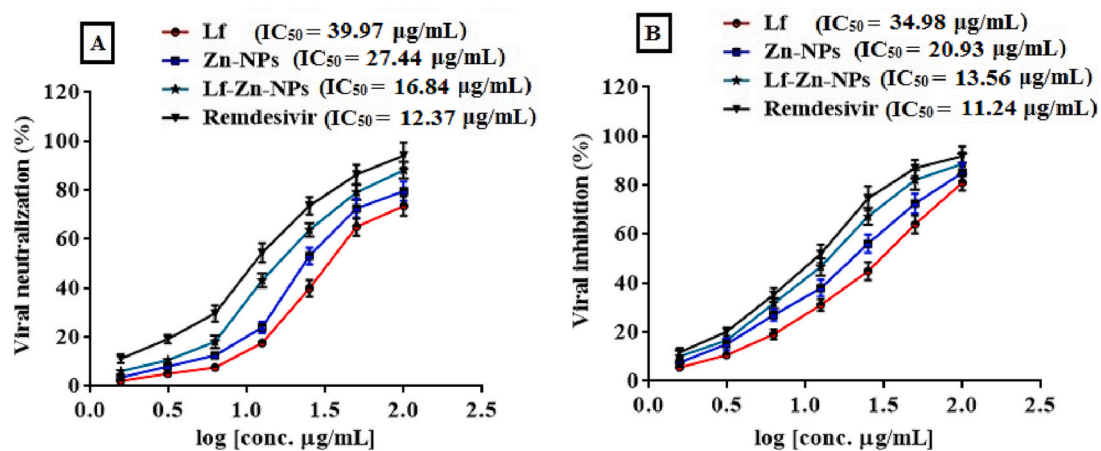

Fig. 6. The antiviral activity of the Lf-Zn-NPs against SARS-CoV-2 *in vitro*. (A) Vero-E6 cells were infected with virus neutralized with Lf, Zn-NPs, Lf-Zn-NPs and remdesivir at different concentrations. (B) Vero-E6 cells were infected with virus for 1 h and then exposed to with Lf, Zn-NPs and Lf-Zn-NPs at different concentrations (0–100 μg/mL, 2 fold) as post-infection mode. The supernatants were harvested after 48 h of treatment and the virus titre were analyzed by qRT-PCR (B). The data are the mean ± SE, at $n = 3$.
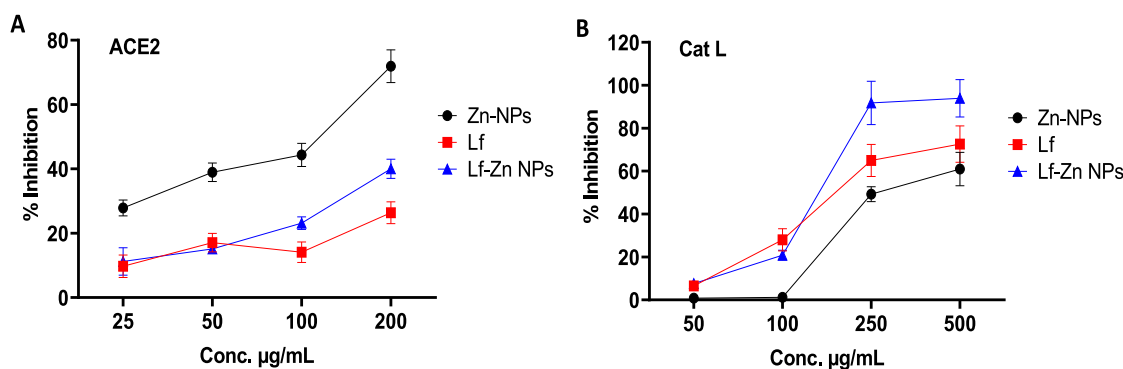
Fig. 7. The ACE2-SARS-CoV-2 spike inhibitor evaluation (A) for Zn NPs, Lf, and Lf-Zn-NPs at different concentrations (25–200 μg/mL), where (B) is the inhibitory activities of Zn-NPs, Lf, and Lf-Zn-NPs at four concentrations (50–500 μg/mL) against Cathepsin L (Cat L). Results are expressed as mean ± standard error. *$p < 0.05$. The data are the mean ± SE, at $n = 3$.

Table 2
Inhibition of RdRp activity by Zn-NPs and Lf combination at different concentrations as compared to Remdesivir as standard antiviral drug.

Conc. μg/mL	Zn-NPs	Lf	Lf-Zn-NPs	Remdesivir
100.00	92.9 ± 11.8	96.61 ± 9.8	94.57 ± 7.3	91.78 ± 7.45
50.00	76.19 ± 3.5	71.68 ± 6.77	68.97 ± 4.75	78.42 ± 2.8
25.00	51.88 ± 7.1	58.89 ± 8.4	51.47 ± 4.0	57.12 ± 7.6
12.50	35.52 ± 4.2	41.79 ± 1.25	34.52 ± 4.25	53.41 ± 9.3
6.25	25.54 ± 6.1	24.42 ± 11.8	19.03 ± 5.35	49.63 ± 2.6
0	00 ± 00	00 ± 00	00 ± 00	00 ± 00
IC$_{50}$	31.79 ± 4.6	35.88 ± 6.23	28.29 ± 2.36	67.52 ± 5.31
Significance	b	c	a	d

Data are expressed as mean ± SD; data were subjected to one-way ANOVA followed by *post hoc* (Tukey) test at p ≤ 0.05. Within each column, means with different superscript letters are significantly different.

Table 3
Effect of Lf-Zn-NPs on the levels of whole blood in induced pulmonary fibrosis (PF) rats as indicated in the healthy group (control), pulmonary fibrosis-modeled (BLM), BLM treated with Lf (BLM-Lf), BLM treated with Zn-NPs (BLM-Zn-NPs), and BLM treated with Lf-Zn-NPs (BLM-Lf-Zn-NPs).

Hematological parameters	Control	BLM	BLM-Lf	BLM-Zn-NPs	BLM-Lf-Zn-NPs
Hb (g/dL)	13.1 ± 0.53	10.82 ± 0.18*	11.9 ± 0.71#	12.1 ± 0.93#	12.5 ± 0.81#
HCT (%)	39.6 ± 1.7	31.5 ± 0.55*	34.1 ± 1.03#	35.9 ± 1.5#	37.1 ± 2.3#
RBC (10^6/μL)	6.4 ± 0.2	4.7 ± 0.32*	5.0 ± 0.51#	5.3 ± 0.16#	5.9 ± 0.17#
WBC (10^3/μL)	6.88 ± 0.88	14.33 ± 2.7*	9.2 ± 3.1#	8.7 ± 1.1#	7.9 ± 2.1#
PLT (10^3/μL)	914 ± 52	1020 ± 79*	843 ± 90#	753 ± 103#	905 ± 110#

Data are expressed as mean ± standard SD; data were subjected to one-way ANOVA followed by *post hoc* (Turkey) test at $p \leq 0.05$. (*) is significantly different from the control group; (#) is significantly different from the BLM group.

delivery (improving solubility), due to their distinctive physical properties in addition to their ability to encapsulate various drug types [47]. Drug-loaded NPs have become one of the most promising drug formulation technologies for targeted therapy due to their capacity to overcome drug resistance with enhanced pharmacokinetics and biodistribution. In this regard, the current study evaluated Zn-NPs' potential to facilitate the internalization of Lf and interfere with SARS-CoV-2 infection.

First, the Lf was purified from bovine milk through several chromatographic steps and evaluated through SDS-PAGE. The results indicated a single protein band at 80 kDa, which is in line with [48,49]. On

the other hand, the green Zn-NPs were successfully prepared on the nanoscale (55.91 nm) through ascorbic acid, as confirmed by SEM results. Several studies attributed the ability of various plant extracts for ZA reduction to Zn-NPs to their contents of ascorbic acid [50,51]. Different recipes were evaluated for the maximum formulation of the isolated Lf protein on the Zn-NPs surfaces. One of the most important characteristics of the NPs is their ability to accumulate protein molecules (protein corona structure), which could be attributed to their large surface-to-volume ratio and surface charges [52,53]. The nano-formulation of Lf on the Zn-NPs was confirmed by measuring their hydrodynamic size, which was 4.13-fold higher (230.8 nm) than pristine Zn-NPs, which could be attributed to the protein layer surrounding the particles [28]. Additionally, the surface charge of the new nano-formulation possessed higher negative charges (−36.85 mV) compared to that of Zn-NPs (−21.62 mV), which supports the combination of Zn-NPs with Lf protein [44]. The increase in negative charges on the nano-complex reduces the aggregation tendency between Zn-NPs, which enhances their structure stability [27].

Additionally, coating the purified Lf into Zn-NPs surface significantly reduced the NPs toxicity compared to free Zn-NPs. Vallhov et al., reported that 3 EU/mL of endotoxin is required to trigger the cellular immune response [54], which asserted the higher safety of the prepared Lf-Zn-NPs in the current study. This result was in line with Nayak et al., [44] who revealed that the toxicity of silver-NPs was reduced after loading with Lf. With the reported toxicity of Zn-NPs [55], the results significantly highlighted the role of Lf in alleviating such toxicity and increasing the Zn-NPs biocompatibility. The results indicated that the formulation of Lf on the Zn-NPs significantly enhanced the cellular uptake of Lf-Zn-NPs in a time-dependent process, compared to free Lf and Zn-NPs. The nano-complex accumulation was increased over time and maximized after 12 h, which asserted the importance of the protein coating process for efficient NPs internalization. The mechanism behind NPs' cellular uptake is controversial and is usually attributed to NPs' interaction with cellular macromolecules outside and inside cells [56]. Hence, since this interaction is already exists in the Lf-Zn complex, the internalization rate was higher, which was also reported in the Lf-Ag complex [44]. As an intercellular infectious agent, accumulation inside target cells is a main characteristic of successful antiviral drug design [57].

The present study, was aimed to investigate the action of the biosynthesized Zn-NPs and the nanofabricated Lf-Zn-NPs against SARS-CoV-2. The obtained findings revealed that Lf-Zn-NPs can display a potential virucidal effect on SARS-CoV-2 through their direct neutralization effect or prevention of virus replication after infection. In fact, both Zn-NPs and Lf-Zn-NPs were able to neutralize the infection of SARS-CoV-2 upon entry into Vero E6 cells with IC$_{50}$ values of 27.44 and 16.84 μg/mL, respectively. Furthermore, both Zn-NPs and Lf-Zn-NPs exhibited a potent anti-replication activity against SARS-CoV-2 with
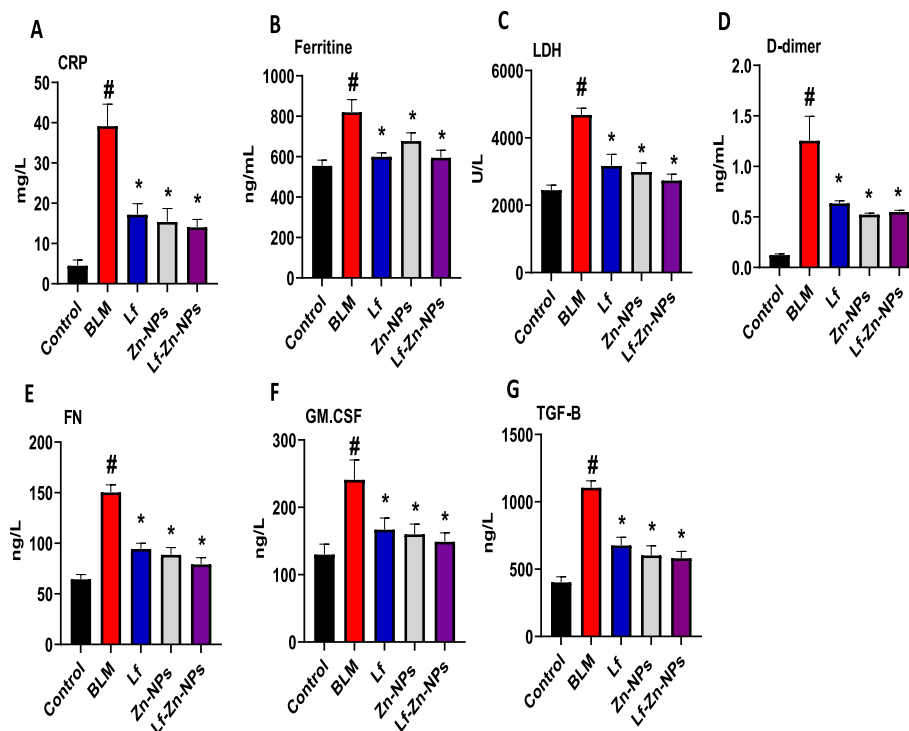
Fig. 8. (A-G). Serum CRP, ferritin, D-dimer, LDH, FN, GM-CSF, and TGF.β of control, pulmonary fibrosis, and pulmonary fibrosis-treated rats. (#) is significantly different from the control group; (*) is significantly different from the Bleomycin group (BLM); Lf: lactoferrin; Zn-NPs: zinc nanoparticles; Lf-Zn-NPs: and lactoferrin-coated zinc nanoparticles.

Table 4
Lung oxidant-antioxidant markers as indicated in the healthy group (control), pulmonary fibrosis-modeled (BLM), BLM rats treated with lactoferrin (BLM-Lf), BLM treated with Zn-NPs (BLM-Zn-NPs), and BLM treated with Lf-Zn-NPs (BLM-Lf-Zn-NPs).

Oxidant-antioxidant markers	Control	BLM	BLM-Lf	BLM-Zn-NPs	BLM-Lf-Zn-NPs
NO (µmol/g)	10.1 ± 0.47	$25.2 \pm 2.1^*$	$16.3 \pm 1.1^\#$	$15.5 \pm 2.1^\#$	$14.6 \pm 3.1^\#$
MDA (µmol/g)	427 ± 28	$887 \pm 43^*$	$557 \pm 35^\#$	$510 \pm 25^\#$	$493 \pm 17^\#$
GSH (nmol/g)	33.2 ± 2.7	$12.11 \pm 1.2^*$	$25.3 \pm 2.7^\#$	$27.1 \pm 3.4^\#$	$29.0 \pm 4.1^\#$
SOD (U/g)	3.2 ± 0.06	$1.4 \pm 0.11^*$	$2.8 \pm 0.22^\#$	$2.9 \pm 0.17^\#$	$3.1 \pm 0.33^\#$
GPx (U/g)	1264 ± 71	$469 \pm 28^*$	$895 \pm 30^\#$	$950 \pm 41^\#$	$1065 \pm 45^\#$
CAT (U/g)	25 ± 1.8	$10.4 \pm 1.2^*$	$17.3 \pm 2.1^\#$	$18.9 \pm 3.1^\#$	$20.3 \pm 4.1^\#$

Data are presented as mean ± standard error; data were subjected to one-way ANOVA followed by *post hoc* (Turkey) test at $p \leq 0.05$. (*) is significantly different from the control group; (#) is significantly different from the Bleomycin group.

IC_{50} values of 20.93 and 13.56 µg/mL, respectively.

Preventing SARS-CoV-2 entry by inhibiting the binding of the virus spike to host ACE2 is one of the approaches in drug design for the treatment of COVID-19 [58]. The ability of Zn-NPs to inhibit the binding between the recognition binding domain (RBD) of the SARS-CoV-2 spike and host ACE2 receptors in a dose-dependent manner was demonstrated in this study (IC_{50} of 89.73 ± 1.59 µg/mL), which is in line with other studies [59,60], and could be attributed to the high affinity of Zn to ACE2 receptors. Furthermore, Lf was reported to prevent SARS-CoV-2 entry into host cells through binding of its N-terminal to Heparan Sulfate Proteoglycans (HSPGs), which is a major viral-binding receptor

[18,61,62], which could elucidate the lower ACE2 inhibition activity of the Lf-Zn complex (IC_{50} of 334 ± 2.23 µg/mL) compared to free Zn-NPs. On the other hand, the results indicated a significant inhibitory effect of Lf-Zn-NPs against Cat L (IC_{50} of 139.6 µg/mL) compared to Zn-NPs and free Lf. Cat L is a viral protease that facilitates the cleavage of the viral spike glycoprotein's S1 component to inject the viral RNA inside the host cells for subsequent replication [63,64]. Several studies reported the ability of Lf to target Cat L activity, especially through the carboxyl-terminal lobe of the intact Lf structure [65,66]. Furthermore, the RdRp proteins are well-known targets for antiviral drugs in most RNA viruses, with several antiviral drugs already in clinical trials [67]. The results asserted the ability of Lf-coated Zn-NPs to interfere with and arrest viral replication by suppressing the enzymatic activity of SARS-CoV-2 RdRp at lower concentrations compared to remdesivir as a standard antiviral drug and free Lf or Zn-NPs.

PF is a deadly and progressive lung disorder that is a main characteristic of severe COVID infection [68]. However, a few drugs are available for PF treatment, and even with limited efficiency [69]. Hence, the current study evaluated the Lf-Zn-NPs' ability to prevent or alleviate the PF progress in the Bleomycin-induced PF-modeled rats. In the BLM-untreated group, the results indicated significant deteriorations in all hematological measurements (reduced RBCs and HCT levels, with an increase of WBCs, and platelets count) leading to a condition of hypochromic-microcytic anemia that resulted in a dependent degree of tissue hypoxia, especially heart and brain tissues, which is in line with other studies [70,71]. BLM directly binds with Fe^{+2}, thereby causing iron deficiency and anemia, whereas it indirectly activates the production of reactive oxygen species (ROS). The BLM-Fe complex can bind to the DNA helix and initiate membrane lipid peroxidation [72]. Lf is a glycoprotein that binds to two iron ions with high affinity and increases iron absorption by intestinal cells, where it is released from Lf and transported to circulation *via* transferrin [73].

In the present study, BLM administration significantly increased the CRP, ferritin, D-dimer, LDH, FN, GM-CSF, and TGF.β; this result is in accordance with other studies [74]. The TGF-β is the master regulator of
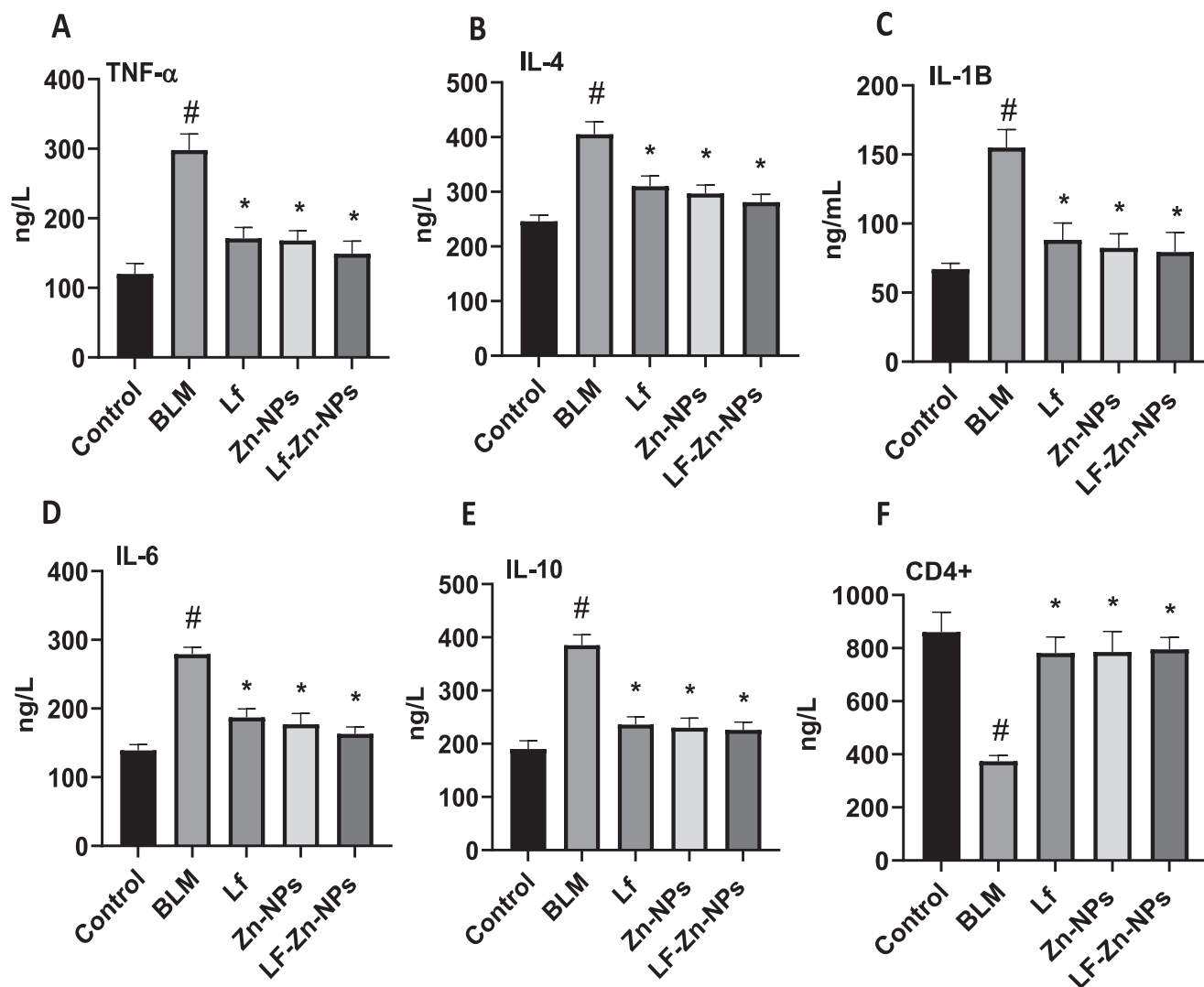
Fig. 9. (A-F). Serum TNF-α, IL-1β, IL-4, IL-6, IL-10, and CD4+ of control, pulmonary fibrosis, and pulmonary fibrosis-treated rats. (#) is significantly different from control group; (*) is significantly different from Bleomycin group; Lf: lactoferrin; Zn-NPs: zinc nanoparticles; Lf-Zn-NPs: lactoferrin-coated zinc nanoparticles; BLM: Bleomycin.

fibrosis and is shown to be upregulated in the lung during fibrosis [75]. The results showed that lactoferrin, Zn-NPs, or Lf-Zn-NPs cause a protective effect against lung fibrosis by both inhibiting TGF-β production and modulating the critical fibrogenic pathways downstream of TGF-β. The BLM-induced PF group revealed significant increases in oxidative potential (MDA and NO) with a significant reduction in the antioxidant enzymes compared to the control group, which agrees with previous results, demonstrating that BLM induces pulmonary injury *via* oxidative stress [76]. Several studies in humans and animals have revealed that hyperoxia and ROS adversely alter innate immunity and increase the risk of pneumonia [77,78]. In association, the overproduction of NO has been demonstrated to play a key role in the induction of pulmonary fibrosis in animal models and humans [79]. Treatment with BLM also increased (TNF-α), IL-1β, IL-4, IL-6, and IL-10, matched with a significant decrease in CD4+, reliable markers of inflammation in pulmonary fibrosis. The therapeutic effects of Lf, Zn-NPs, or Lf-Zn-NPs against BLM-induced pulmonary fibrosis could be due to their antioxidative, anti-inflammatory, immunomodulatory, and anti-apoptotic properties. Lactoferrin, an iron-binding protein of the transferrin family with a high affinity for iron, inhibits ROS overproduction due to its iron-binding capacity, as iron promotes hydroxyl radical formation and lipid oxidation during inflammation [80–82]. The anti-inflammatory effect of Lf

NPs is mainly attributed to its significant role in the induction of anti-inflammatory cytokines interleukin (IL)-4, (IL)-6, and IL-10 and reductions in the pro-inflammatory cytokines tumor's necrosis factor-α and IL-1β by suppressing the NF-κB signaling pathway [83]. Also, Lf-loaded NPs have been reported to promote the macrophage shift from an inflammatory to a tolerogenic phenotype, which is key for tissue homeostasis [84]. In addition, Lf NPs can reduce oxidative stress-induced apoptosis by decreasing the intracellular levels of ROS [85]. Moreover, Lf NPs antioxidant activity is most likely related to its iron-scavenging ability and inhibition of iron-catalyzed ROS formation [81,82]. Furthermore, Lf NPs enhance the proliferation, differentiation, maturation, migration, and function of immune cells [86]. The biochemical results are confirmed by the histopathological examination, which proved that BLM causes PF-marked alveolar wall thickness, fibrosis, inflammatory cells, and lymphoid aggregates. Also, the lung interstitium is disturbed with areas of hemorrhage, which is supported by another previous study [70]. The pathological importance of oxidative stress and ROS in BLM has been highlighted by previous studies [87], by targeting macromolecules, leading to higher rates of lipid peroxidation [87]. Lf, Zn-NPs, or Lf-Zn-NPs treatment effectively alleviated the BLM-induced pulmonary fibrosis histopathological changes; the pharmacological potential of LFNPs against various pathological
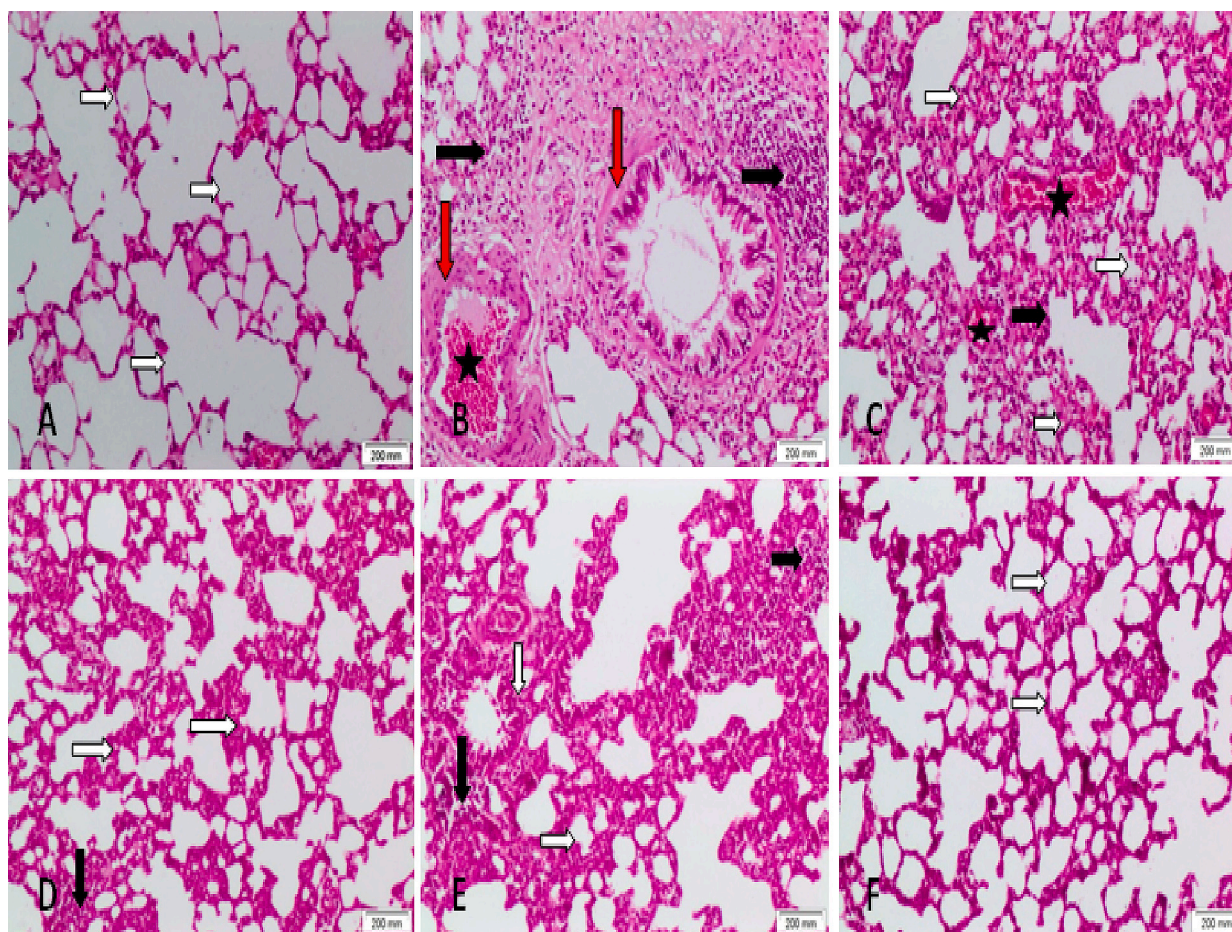
Fig. 10. Photomicrographs of lung tissue revealing the normal control group (A). The BLM-treated group (B and C) showed marked alveolar wall thickness, fibrosis, inflammatory cells, and lymphoid aggregates, also the lung interstitium is disturbed with areas of hemorrhage. The lactoferrin-treated + BLM animals (D) showed normal lung structure with increased alveolar wall thickness and scattered inflammatory cells. The Zn-NPs-treated + BLM animals (E) revealed normal lung structure with increased alveolar wall thickness and scattered inflammatory cells and minimal fibrosis. The Lf-Zn-NPs-treated + BLM group (F) revealed normal lung structure. White arrow: the thickness of the alveolar wall. Black arrow: inflammation. Red arrow: fibrosis. Star: hemorrhage (H&E ×100).

Table 5
Scoring of fibrosis and inflammation of lung tissues in treated pulmonary-fibrosis modeled animal groups as compared to control animals.

	Control	BLM	BLM-Lf	BLM-Zn-NPs	BLM-Lf-Zn-NPs
Congestion	0.16 ± 0.018	2.83 ± 0.18*	0.66 ± 0.22#	0.83 ± 0.18#	0.33 ± 0.18#
Inflammation	0.16 ± 0.018	2.83 ± 0.18*	0.66 ± 0.36#	1.5 ± 0.22#	0.2 ± 0.22#
Alveolar thickness	0.0 ± 0.0	3.0 ± 0.0*	0.66 ± 0.22#	1.0 ± 0.78#	0.0 ± 0.0#
Fibrosis	0.0 ± 0.0	2.8 ± 0.18*	0.66 ± 0.22#	0.83 ± 0.38#	0.0 ± 0.0#

Data are presented as mean ± standard error; data were subjected to a one-way ANOVA followed by *post hoc* (Turkey) test at p ≤ 0.05. (*) is significantly different from control group; (#) is significantly different from BLM group; Lf: lactoferrin; Zn-NPs: zinc nanoparticles; Lf-Zn-NPs: lactoferrin-coated zinc nanoparticles; BLM: Bleomycin.

conditions, including oxidative stress, inflammation, fibrosis, ER stress, autophagy dysfunction, and mitochondrial dysfunction.

5. Conclusion

In the current study, Zn-NPs were synthesized by ascorbic acid in a green approach and coated into the purified lactoferrin (Lf-Zn-NPs) for using as a potential antiviral drug against SARS-CoV-2 and antifibrotic agents to alleviate pulmonary fibrosis in rats. The formation of NPs was confirmed through instrumental analysis, revealing Zn-NPs in the range of 55.91 nm with a Zeta-potential of −21.62 mV, which proved the applicability of ascorbic acid as a potent reducer for Zn-NPs preparation. Additionally, nanofabrication of the purified Lf with Zn-NPs was also confirmed by increasing their particle size with lower zeta-potentials (230.8 nm and −36.85 mV, respectively). The *in vitro* studies revealed the significant impact of Lf-Zn-NPs accumulation in target cells with lower endotoxin properties, which pave the way for safer application of Lf-Zn-NPs. The Lf-Zn-NPs revealed significant *in vitro* antiviral activity against SARS-CoV-2 by interfering with viral entry by binding to the ACE2 receptor and inactivating viral replication through the inactivation of RdRp. Furthermore, Lf-Zn-NPs revealed significant *in vivo* potential to alleviate the Bleomycin-induced pulmonary fibrosis (PF) in White albino rats by reducing the generated oxidative stress and overexpressed inflammatory and modulatory cytokines, which proves the applicability of Lf-Zn-NPs for prophylactic and acute-infection treatment of COVID-19 infections. Therefore, this study provided evidence that the anti-viral treatment feature of Lf-Zn-NPs may offer a novel alternative therapy for the treatment of PF through enhancement of the apoptosis pathway, improvement of the immune response, reduction of inflammation, and restoration of impaired oxidative stress.

Ethics approval and consent to participate

All methods were performed in accordance with the relevant guidelines and regulations, and the experiments done on animals were in accordance with the guidelines. The experimental design was accepted by the local research ethical committee (REC) for experimental animal use at the National Research Centre, Cairo, Egypt, by applying the principles of replacement, reduction, and refinement (the 3Rs).

Consent for publication

Not applicable.

Availability of data and materials

All data generated or analyzed during this study are included in this published article.

CRediT authorship contribution statement

Esmail M. El-Fakharany: Conceptualization, methodology, writing - original draft, writing - review & editing, software, data curation, validation, visualization. **Hamada El-Gendi**: Methodology, writing - review & editing, software, data curation, validation, visualization. **Yousra A. El-Maradny**: Methodology, writing - review & editing, software, data curation, validation, visualization. **Marwa M. Abu-Serie**: Conceptualization, methodology, writing - review & editing, validation, visualization, **Khaled G. Abdel-Wahhab**: Methodology, writing - original draft, editing, validation, visualization. **Marwa E. Shaban**: Methodology, writing - review & editing, validation, visualization, and **Mahmoud Ashry:** Methodology, writing - review & editing, software, data curation, validation, visualization.

Declaration of competing interest

The authors declare that they have no known competing financial interests or personal relationships that could have appeared to influence the work reported in this paper.

Data availability

Data will be made available on request.

Acknowledgments

References

[1] J. McVernon, J. Liberman, WHO keeps covid-19 a public health emergency of international concern, BMJ 380 (2023), p504, https://doi.org/10.1136/bmj.p504.

[2] C. Del Rio, P.N. Malani, COVID-19 in 2022—the beginning of the end or the end of the beginning? JAMA 327 (2022) 2389–2390.

[3] M. Alexandridi, J. Mazej, E. Palermo, J. Hiscott, The coronavirus pandemic–2022: viruses, variants & vaccines, Cytokine Growth Factor Rev. (2022).

[4] S. Kassirian, R. Taneja, S. Mehta, Diagnosis and management of acute respiratory distress syndrome in a time of COVID-19, Diagnostics 10 (2020) 1053.

[5] H.M. Al-kuraishy, G.E.-S. Batiha, H. Faidah, A.I. Al-Gareeb, H.M. Saad, J. Simal-Gandara, Pirfenidone and post-Covid-19 pulmonary fibrosis: invoked again for realistic goals, Inflammopharmacology 30 (2022) 2017–2026, https://doi.org/10.1007/s10787-022-01027-6.

[6] P.M. George, C.M. Patterson, A.K. Reed, M. Thillai, Lung transplantation for idiopathic pulmonary fibrosis, Lancet Respir. Med. 7 (2019) 271–282.

[7] P.M. George, A.U. Wells, R.G. Jenkins, Pulmonary fibrosis and COVID-19: the potential role for antifibrotic therapy, Lancet Respir. Med. 8 (2020) 807–815, https://doi.org/10.1016/S2213-2600(20)30225-3.

[8] C. Vancheri, M. Failla, N. Crimi, G. Raghu, Idiopathic pulmonary fibrosis: a disease with similarities and links to cancer biology, Eur. Respir. J. 35 (2010) 496–504.

[9] G. Raghu, S.-Y. Chen, W.-S. Yeh, B. Maroni, Q. Li, Y.-C. Lee, H.R. Collard, Idiopathic pulmonary fibrosis in US Medicare beneficiaries aged 65 years and older: incidence, prevalence, and survival, 2001–11, Lancet Respir. Med. 2 (2014) 566–572.

[10] E. Balboni, F. Zagnoli, T. Filippini, S.J. Fairweather-Tait, M. Vinceti, Zinc and selenium supplementation in COVID-19 prevention and treatment: a systematic review of the experimental studies, J. Trace Elem. Med. Biol. 71 (2022), 126956, https://doi.org/10.1016/j.jtemb.2022.126956.

[11] A. Pal, R. Squitti, M. Picozza, A. Pawar, M. Rongioletti, A.K. Dutta, S. Sahoo, K. Goswami, P. Sharma, R. Prasad, Zinc and COVID-19: basis of current clinical trials, Biol. Trace Elem. Res. 199 (2021) 2882–2892, https://doi.org/10.1007/s12011-020-02437-9.

[12] M. Zimecki, J.K. Actor, M.L. Kruzel, The potential for Lactoferrin to reduce SARS-CoV-2 induced cytokine storm, Int. Immunopharmacol. 95 (2021), 107571, https://doi.org/10.1016/j.intimp.2021.107571.

[13] S.A. González-Chávez, S. Arévalo-Gallegos, Q. Rascón-Cruz, Lactoferrin: structure, function and applications, Int. J. Antimicrob. Agents 33 (2009) 301–e1.

[14] U. Regueiro, M. López-López, R. Varela-Fernández, F.J. Otero-Espinar, I. Lema, Biomedical applications of lactoferrin on the ocular surface, Pharmaceutics 15 (2023) 865.

[15] Y. Wei, K. Feng, S. Li, T. Hu, R.J. Linhardt, M. Zong, H. Wu, Oral fate and stabilization technologies of lactoferrin: a systematic review, Crit. Rev. Food Sci. Nutr. 62 (2022) 6341–6358.

[16] E.N. Baker, H.M. Baker, Lactoferrin: molecular structure, binding properties and dynamics of lactoferrin, Cell. Mol. Life Sci. 62 (2005) 2531–2539.

[17] M. Bielecka, G. Cichosz, H. Czeczot, Antioxidant, antimicrobial and anticarcinogenic activities of bovine milk proteins and their hydrolysates - a review, Int. Dairy J. 127 (2022), 105208, https://doi.org/10.1016/j.idairyj.2021.105208.

[18] Y. Hu, X. Meng, F. Zhang, Y. Xiang, J. Wang, The in vitro antiviral activity of lactoferrin against common human coronaviruses and SARS-CoV-2 is mediated by targeting the heparan sulfate co-receptor, Emerg. Microbes Infect. 10 (2021) 317–330.

[19] B.-L. Waarts, O.J.C. Aneke, J.M. Smit, K. Kimata, R. Bittman, D.K.F. Meijer, J. Wilschut, Antiviral activity of human lactoferrin: inhibition of alphavirus interaction with heparan sulfate, Virology 333 (2005) 284–292, https://doi.org/10.1016/j.virol.2005.01.010.

[20] T. Takeuchi, T. Jyonotsuka, N. Kamemori, G. Kawano, H. Shimizu, K. Ando, E. Harada, Enteric-formulated lactoferrin was more effectively transported into blood circulation from gastrointestinal tract in adult rats, Exp. Physiol. 91 (2006) 1033–1040.

[21] A.O. Elzoghby, M.A. Abdelmoneem, I.A. Hassanin, M.M. Abd Elwakil, M.A. Elnaggar, S. Mokhtar, J.-Y. Fang, K.A. Elkhodairy, Lactoferrin, a multi-functional glycoprotein: active therapeutic, drug nanocarrier & targeting ligand, Biomaterials. 263 (2020) 120355, https://doi.org/10.1016/j.biomaterials.2020.120355.

[22] R. Kumar, N. Varshney, S. Mahapatra, S.K. Mahto, V.K. Dubey, P. Chandra, Design and development of lactoferrin conjugated lipid-polymer nano-bio-hybrid for cancer theranostics, Mater. Today Commun. 31 (2022), 103548, https://doi.org/10.1016/j.mtcomm.2022.103548.

[23] F. Moradian, S. Mohammadzadeh, Evaluation of the effect of nano-encapsulated lactoferrin on the expression of Bak and Bax genes in gastric cancer cell line AGS and study of the molecular docking of lactoferrin with these proteins, Gene. 866 (2023), 147355, https://doi.org/10.1016/j.gene.2023.147355.

[24] R. Varela-Fernández, X. García-Otero, V. Díaz-Tomé, U. Regueiro, M. López-López, M. González-Barcia, M. Isabel Lema, F. Javier Otero-Espinar, Lactoferrin-loaded nanostructured lipid carriers (NLCs) as a new formulation for optimized ocular drug delivery, Eur. J. Pharm. Biopharm. 172 (2022) 144–156, https://doi.org/10.1016/j.ejpb.2022.02.010.

[25] V. Chandrakala, V. Aruna, G. Angajala, Review on metal nanoparticles as nanocarriers: current challenges and perspectives in drug delivery systems, Emergent Mater. 5 (2022) 1593–1615, https://doi.org/10.1007/s42247-021-00335-x.

[26] M. Chelladurai, G. Margavelu, S. Vijayakumar, Z.I. González-Sánchez, K. Vijayan, R. Sahadevan, Preparation and characterization of amine-functionalized mupirocin-loaded zinc oxide nanoparticles: a potent drug delivery agent in targeting human epidermoid carcinoma (A431) cells, J. Drug Deliv. Sci. Technol. 70 (2022), 103244, https://doi.org/10.1016/j.jddst.2022.103244.

[27] E.M. El-Fakharany, Nanoformulation of lactoferrin potentiates its activity and enhances novel biotechnological applications, Int. J. Biol. Macromol. 165 (2020) 970–984, https://doi.org/10.1016/j.ijbiomac.2020.09.235.

[28] J. Piella, N.G. Bastús, V. Puntes, Size-dependent protein–nanoparticle interactions in citrate-stabilized gold nanoparticles: the emergence of the protein corona, Bioconjug. Chem. 28 (2017) 88–97.

[29] P.J.P. Espitia, N. de F.F. Soares, J.S. dos R. Coimbra, N.J. de Andrade, R.S. Cruz, E.A. Medeiros, Zinc oxide nanoparticles: synthesis, antimicrobial activity and food packaging applications, Food Bioprocess Technol. 5 (2012) 1447–1464.

[30] M.H. Kahsay, A. Tadesse, D. RamaDevi, N. Belachew, K. Basavaiah, Green synthesis of zinc oxide nanostructures and investigation of their photocatalytic and bactericidal applications, RSC Adv. 9 (2019) 36967–36981.

[31] H.S. Hassan, H. Abol-Fotouh, E. Salama, M.F. Elkady, Assessment of antimicrobial, cytotoxicity, and antiviral impact of a green zinc oxide/activated carbon nanocomposite, Sci. Rep. 12 (2022) 8774.

[32] P. Merkl, S. Long, G.M. McInerney, G.A. Sotiriou, Antiviral activity of silver, copper oxide and zinc oxide nanoparticle coatings against SARS-CoV-2, Nanomaterials 11 (2021) 1312.

[33] J. Gupta, M. Irfan, N. Ramgir, K.P. Muthe, A.K. Debnath, S. Ansari, J. Gandhi, C.T. Ranjith-Kumar, M. Surjit, Antiviral activity of zinc oxide nanoparticles and

tetrapods against the hepatitis E and hepatitis C viruses, Front. Microbiol. 13 (2022).

[34] H. Ghaffari, A. Tavakoli, A. Moradi, A. Tabarraei, F. Bokharaei-Salim, M. Zahmatkeshan, M. Farahmand, D. Javanmard, S.J. Kiani, M. Esghaei, Inhibition of H1N1 influenza virus infection by zinc oxide nanoparticles: another emerging application of nanomedicine, J. Biomed. Sci. 26 (2019) 1–10.

[35] M. Canta, V. Cauda, The investigation of the parameters affecting the ZnO nanoparticle cytotoxicity behaviour: a tutorial review, Biomater. Sci. 8 (2020) 6157–6174.

[36] O. Almahdy, E.M. El-Fakharany, E.-D. Ehab, T.B. Ng, E.M. Redwan, Examination of the activity of camel milk casein against hepatitis C virus (genotype-4a) and its apoptotic potential in hepatoma and hela cell lines, Hepat. Mon. 11 (2011) 724.

[37] E. El-Fakharany, A. Tabll, A. Wahab, B. Haroun, E.-R. Redwan, Potential activity of camel milk-amylase and lactoferrin against hepatitis C virus infectivity in HepG2 and lymphocytes, Hepat. Mon. 8 (2008) 101–109.

[38] E.M. El-Fakharany, L. Sánchez, H.A. Al-Mehdar, E.M. Redwan, Effectiveness of human, camel, bovine and sheep lactoferrin on the hepatitis C virus cellular infectivity: comparison study, Virol. J. 10 (2013) 1–10.

[39] H. Wakabayashi, K. Yamauchi, T. Kobayashi, T. Yaeshima, K. Iwatsuki, H. Yoshie, Inhibitory effects of lactoferrin on growth and biofilm formation of Porphyromonas gingivalis and Prevotella intermedia, Antimicrob. Agents Chemother. 53 (2009) 3308–3316.

[40] M.M. Bradford, A rapid and sensitive method for the quantitation of microgram quantities of protein utilizing the principle of protein-dye binding, Anal. Biochem. 72 (1976) 248–254.

[41] U.K. Laemmli, Cleavage of structural proteins during the assembly of the head of bacteriophage T4, Nature. 227 (1970) 680–685.

[42] N. Chaithanatkun, D. Chantarawong, P. Songkeaw, K. Onlaor, T. Thiwawong, B. Tunhoo, Effect of ascorbic acid on structural properties of ZnO nanoparticles prepared by precipitation process, in: 10th IEEE Int. Conf. Nano/Micro Eng. Mol. Syst, IEEE, 2015, pp. 145–148.

[43] P. Goldoni, L. Sinibaldi, P. Valenti, N. Orsi, Metal complexes of lactoferrin and their effect on the intracellular multiplication of Legionella pneumophila, Biometals. 13 (2000) 15–22, https://doi.org/10.1023/A:1009221616623.

[44] P.S. Nayak, S.M. Borah, H. Gogoi, S. Asthana, R. Bhatnagar, A.N. Jha, S. Jha, Lactoferrin adsorption onto silver nanoparticle interface: implications of corona on protein conformation, nanoparticle cytotoxicity and the formulation adjuvanticity, Chem. Eng. J. 361 (2019) 470–484.

[45] A. Carino, F. Moraca, B. Fiorillo, S. Marchianò, V. Sepe, M. Biagioli, C. Finamore, S. Bozza, D. Francisci, E. Distrutti, Hijacking SARS-CoV-2/ACE2 receptor interaction by natural and semi-synthetic steroidal agents acting on functional pockets on the receptor binding domain, Front. Chem. 8 (2020), 572885.

[46] R. Akgedik, Ş. Akgedik, H. Karamanlı, S. Uysal, B. Bozkurt, D. Ozol, F. Armutcu, Z. Yıldırım, Effect of resveratrol on treatment of bleomycin-induced pulmonary fibrosis in rats, Inflammation 35 (2012) 1732–1741.

[47] L. Singh, H.G. Kruger, G.E.M. Maguire, T. Govender, R. Parboosing, The role of nanotechnology in the treatment of viral infections, Ther. Adv. Infect. Dis. 4 (2017) 105–131.

[48] C. Conesa, L. Sánchez, C. Rota, M.-D. Pérez, M. Calvo, S. Farnaud, R.W. Evans, Isolation of lactoferrin from milk of different species: calorimetric and antimicrobial studies, Comp. Biochem. Physiol. Part B Biochem. Mol. Biol. 150 (2008) 131–139, https://doi.org/10.1016/j.cbpb.2008.02.005.

[49] T.P. Hopp, K. Spiewak, M.-A.H. Matthews, Z. Athanasiou, R.S. Blackmore, G. A. Gelbfish, Characterization of proteolytic degradation products of vaginally administered bovine lactoferrin, PLoS One 17 (2022), e0268537.

[50] A. Abbasifar, F. Shahrabadi, B. ValizadehKaji, Effects of green synthesized zinc and copper nano-fertilizers on the morphological and biochemical attributes of basil plant, J. Plant Nutr. 43 (2020) 1104–1118.

[51] A. Taşdemir, N. Akman, A. Akkaya, R. Aydın, B. Şahin, Green and cost-effective synthesis of zinc oxide thin films by L-ascorbic acid (AA) and their potential for electronics and antibacterial applications, Ceram. Int. 48 (2022) 10164–10173, https://doi.org/10.1016/j.ceramint.2021.12.228.

[52] M. Farshbaf, H. Valizadeh, Y. Panahi, Y. Fatahi, M. Chen, A. Zarebkohan, H. Gao, The impact of protein corona on the biological behavior of targeting nanomedicines, Int. J. Pharm. 614 (2022) 121458, https://doi.org/10.1016/j.ijpharm.2022.121458.

[53] S. Khan, M. Sharifi, J.P. Gleghorn, M.M.N. Babadaei, S.H. Bloukh, Z. Edis, M. Amin, Q. Bai, T.L.M. ten Hagen, M. Falahati, W.C. Cho, Artificial engineering of the protein corona at bio-nano interfaces for improved cancer-targeted nanotherapy, J. Control. Release 348 (2022) 127–147, https://doi.org/10.1016/j.jconrel.2022.05.055.

[54] H. Vallhov, J. Qin, S.M. Johansson, N. Ahlborg, M.A. Muhammed, A. Scheynius, S. Gabrielsson, The importance of an endotoxin-free environment during the production of nanoparticles used in medical applications, Nano Lett. 6 (2006) 1682–1686.

[55] A. Czyżowska, A. Barbasz, Cytotoxicity of zinc oxide nanoparticles to innate and adaptive human immune cells, J. Appl. Toxicol. 41 (2021) 1425–1437.

[56] E. Casals, T. Pfaller, A. Duschl, G.J. Oostingh, V. Puntes, Time evolution of the nanoparticle protein corona, ACS Nano 4 (2010) 3623–3632.

[57] N. Anand, R. Sehgal, R.K. Kanwar, M.L. Dubey, R.K. Vasishta, J.R. Kanwar, Oral administration of encapsulated bovine lactoferrin protein nanocapsules against intracellular parasite Toxoplasma gondii, Int. J. Nanomedicine 10 (2015) 6355–6369, https://doi.org/10.2147/IJN.S85286.

[58] I. Ahmad, R. Pawara, S. Surana, H. Patel, The repurposed ACE2 inhibitors: SARS-CoV-2 entry blockers of Covid-19, Top. Curr. Chem. 379 (2021) 40, https://doi.org/10.1007/s41061-021-00353-7.

[59] R. Speth, E. Carrera, M. Jean-Baptiste, A. Joachim, A. Linares, Concentration-dependent effects of zinc on angiotensin-converting enzyme-2 activity (1067.4), FASEB J. 28 (2014) 1064–1067.

[60] P.R. Fatouros, U. Roy, S. Sur, Modeling substrate coordination to Zn-bound angiotensin converting enzyme 2, Int. J. Pept. Res. Ther. 28 (2022) 65.

[61] Y. Wang, P. Wang, H. Wang, Y. Luo, L. Wan, M. Jiang, Y. Chu, Lactoferrin for the treatment of COVID-19, Exp. Ther. Med. 20 (2020) 1.

[62] E. Campione, C. Lanna, T. Cosio, L. Rosa, M.P. Conte, F. Iacovelli, A. Romeo, M. Falconi, C. Del Vecchio, E. Franchin, M.S. Lia, M. Minieri, C. Chiaramonte, M. Ciotti, M. Nuccetelli, A. Terrinoni, I. Iannuzzi, L. Coppeda, A. Magrini, S. Bernardini, S. Sabatini, F. Rosapepe, P.L. Bartoletti, N. Moricca, A. Di Lorenzo, M. Andreoni, L. Sarmati, A. Miani, P. Piscitelli, P. Valenti, L. Bianchi, Lactoferrin against SARS-CoV-2: in vitro and in silico evidences, Front. Pharmacol. 12 (2021) 1–10, https://doi.org/10.3389/fphar.2021.666600.

[63] T. Liu, S. Luo, P. Libby, G.-P. Shi, Cathepsin L-selective inhibitors: a potentially promising treatment for COVID-19 patients, Pharmacol. Ther. 213 (2020), 107587.

[64] A. Pišlar, A. Mitrović, J. Sabotič, U. Pečar Fonović, M. Perišić Nanut, T. Jakoš, E. Senjor, J. Kos, The role of cysteine peptidases in coronavirus cell entry and replication: the therapeutic potential of cathepsin inhibitors, PLoS Pathog. 16 (2020), e1009013.

[65] D. Patil, S. Chen, V. Fogliano, A. Madadlou, Hydrolysis improves the inhibition efficacy of bovine lactoferrin against infection by SARS-CoV-2 pseudovirus, Int. Dairy J. 137 (2023), 105488.

[66] A. Madadlou, Food proteins are a potential resource for mining cathepsin L inhibitory drugs to combat SARS-CoV-2, Eur. J. Pharmacol. 885 (2020), 173499.

[67] R.H. Pirzada, M. Haseeb, M. Batool, M. Kim, S. Choi, Remdesivir and ledipasvir among the FDA-approved antiviral drugs have potential to inhibit SARS-CoV-2 replication, Cells. 10 (2021) 1052.

[68] D.J. Leeming, F. Genovese, J.M.B. Sand, D.G.K. Rasmussen, C. Christiansen, G. Jenkins, T.M. Maher, J. Vestbo, M.A. Karsdal, Can biomarkers of extracellular matrix remodelling and wound healing be used to identify high risk patients infected with SARS-CoV-2?: lessons learned from pulmonary fibrosis, Respir. Res. 22 (2021) 38, https://doi.org/10.1186/s12931-020-01590-y.

[69] S. Puglisi, S.E. Torrisi, V. Vindigni, R. Giuliano, S. Palmucci, M. Mulè, C. Vancheri, New perspectives on management of idiopathic pulmonary fibrosis, Ther. Adv. Chronic Dis. 7 (2016) 108–120.

[70] D.M. Zakaria, N.M. Zahran, S.A.A. Arafa, R.A. Mehanna, R.A. Abdel-Moneim, Histological and physiological studies of the effect of bone marrow-derived mesenchymal stem cells on bleomycin induced lung fibrosis in adult albino rats, Tissue Eng. Regen. Med. 18 (2021) 127–141.

[71] S. Maimonaparveen, D. Madhuri, M. Lakshman, B. Anilkumar, M.L. Namratha, Y. Ravikumar, K. Sandhyarani, Effect of Bleomycin (BLM) Induced Toxicity on Body Weights and Hematological Parameters and Protective Role of Whole Pomegranate Juice in Rats, 2021.

[72] A. Allawzi, H. Elajaili, E.F. Redente, E. Nozik-Grayck, Oxidative toxicology of bleomycin: role of the extracellular redox environment, Curr. Opin. Toxicol. 13 (2019) 68–73.

[73] Y.A. Suzuki, B. Lönnerdal, Characterization of mammalian receptors for lactoferrin, Biochem. Cell Biol. 80 (2002) 75–80.

[74] M. Mehdizadeh, H. Farhangi, Corrigendum to "Effects of different elevated temperature and long-term exposure on microstructural evolution and mechanical characteristics of IN617 Ni-based superalloy" [Mater. Sci. Eng. A 841 (2022) 143025] (Materials Science & Engineering A (2022) 841, (S0921509322004324), (10.1016/j.msea.2022.143025)), Mater. Sci. Eng. A (2022), https://doi.org/10.1016/j.msea.2022.143508.

[75] J.A. Lasky, A.R. Brody, Interstitial fibrosis and growth factors, Environ. Health Perspect. 108 (2000) 751–762.

[76] N. Shahabi, S. Mohseni, S. Dadipoor, R.E. Rad, H.K. Takhti, F. Noruziyan, S. Kashani, T. Aghamolaei, Investigating the relationship between health literacy and Covid-19 preventive behaviors: a cross-sectional study in Hormozgan, Iran, J. Heal. Lit. (2023), https://doi.org/10.22038/jhl.2022.65679.1299.

[77] W.A. Altemeier, S.E. Sinclair, Hyperoxia in the intensive care unit: why more is not always better, Curr. Opin. Crit. Care 13 (2007) 73–78.

[78] C.E.O. Baleeiro, S.E. Wilcoxen, S.B. Morris, T.J. Standiford, R. Paine, Sublethal hyperoxia impairs pulmonary innate immunity, J. Immunol. 171 (2003) 955–963.

[79] S. Kalayarasan, N. Sriram, G. Sudhandiran, Diallyl sulfide attenuates bleomycin-induced pulmonary fibrosis: critical role of iNOS, NF-κB, TNF-α and IL-1β, Life Sci. 82 (2008) 1142–1153.

[80] M. Konishi, M. Iwasa, K. Yamauchi, R. Sugimoto, N. Fujita, Y. Kobayashi, S. Watanabe, S. Teraguchi, Y. Adachi, M. Kaito, Lactoferrin inhibits lipid peroxidation in patients with chronic hepatitis C, Hepatol. Res. 36 (2006) 27–32.

[81] M. Tomita, H. Wakabayashi, K. Shin, K. Yamauchi, T. Yaeshima, K. Iwatsuki, Twenty-five years of research on bovine lactoferrin applications, Biochimie. 91 (2009) 52–57.

[82] A. Lawen, D.J.R. Lane, Mammalian iron homeostasis in health and disease: uptake, storage, transport, and molecular mechanisms of action, Antioxid. Redox Signal. 18 (2013) 2473–2507.

[83] J.-I. Togawa, H. Nagase, K. Tanaka, M. Inamori, T. Umezawa, A. Nakajima, M. Naito, S. Sato, T. Saito, H. Sekihara, Lactoferrin reduces colitis in rats via modulation of the immune system and correction of cytokine imbalance, Am. J. Physiol. Liver Physiol. 283 (2002) G187–G195.

[84] A. Cutone, L. Rosa, M.S. Lepanto, M.J. Scotti, F. Berlutti, M.C. Bonaccorsi di Patti, G. Musci, P. Valenti, Lactoferrin efficiently counteracts the inflammation-induced changes of the iron homeostasis system in macrophages, Front. Immunol. 8 (2017) 705.

[85] J.K. Actor, S.-A. Hwang, M.L. Kruzel, Lactoferrin as a natural immune modulator, Curr. Pharm. Des. 15 (2009) 1956–1973.

[86] T. Siqueiros-Cendón, S. Arévalo-Gallegos, B.F. Iglesias-Figueroa, I.A. García-Montoya, J. Salazar-Martínez, Q. Rascón-Cruz, Immunomodulatory effects of lactoferrin, Acta Pharmacol. Sin. 35 (2014) 557–566, https://doi.org/10.1038/aps.2013.200.

[87] M. Kellner, S. Noonepalle, Q. Lu, A. Srivastava, E. Zemskov, S.M. Black, ROS signaling in the pathogenesis of acute lung injury (ALI) and acute respiratory distress syndrome (ARDS), Pulm. Vasc. Redox Signal. Heal. Dis. (2017) 105–137.